AFRL-SR-AR-TR-05-

$0299\ 5$

1. REPORT DATE *(DD–MM–YYYY)*	2. REPORT	TES COVERED *(From — To)*
01-24-2005	Final	ly 2002 — 24 Oct 2004

4. TITLE AND SUBTITLE

Final Report for SYSTEMATIC INVESTIGATION OF BLUFF-BODY COMBUSTION INSTABILITY

5a. ... NUMBER

F49620–02–C–0048

5b. GRANT NUMBER

5c. PROGRAM ELEMENT NUMBER

6. AUTHOR(S)

Godfrey, Andrew (editor)
Vandsburger, Uri
Cliff, Gene

5d. PROJECT NUMBER

5e. TASK NUMBER

5f. WORK UNIT NUMBER

7. PERFORMING ORGANIZATION NAME(S) AND ADDRESS(ES)

AeroSoft, Inc.
1872 Pratt Drive, Suite 1275
Blacksburg, VA 24060–6363

8. PERFORMING ORGANIZATION REPORT NUMBER

9. SPONSORING / MONITORING AGENCY NAME(S) AND ADDRESS(ES)

Air Force Office of Scientific Research
4015 Wilson Blvd., Room 713, Arlington VA 22203

DCMA Southern Virginia
190 Bernard Rd., Bldg 117, Fort Monroe, VA 23651

10. SPONSOR/MONITOR'S ACRONYM(S)

11. SPONSOR/MONITOR'S REPORT NUMBER(S)

12. DISTRIBUTION / AVAILABILITY STATEMENT

Approval for public release; distribution is unlimited.

13. SUPPLEMENTARY NOTES

The views, opinions and/or findings contained in this report are those of the authors and should not be construed as an official U.S. Government position, policy or decision, unless so designated by other documentation.

14. ABSTRACT

The objectives, work carried out and results obtained during a Phase II STTR project are reported. An capability for unsteady flows is added to a sensitivity tool which numerically solves the continuous sensitivity equations. A feedback control law is implemented to control numerically an acoustic instability, which is modeled by coupling pressure and velocity perturbations at an inflow boundary condition. Axi-symmetric simulations are presented for the burner both without methane injection and with five injection locations. The computation is performed using a 12-specie methane/air chemistry model with finite-rate chemical kinetics. An experimental investigation is pursued of a circular bluff-body burner equipped with multiple fuel injectors. The axial injector is used as a pilot flame for premixed observations at equivalence ratios of 0.4 and 0.5.

15. SUBJECT TERMS

Sensitivity equations; Combustion instability

16. SECURITY CLASSIFICATION OF:			17. LIMITATION OF ABSTRACT	18. NUMBER OF PAGES	19a. NAME OF RESPONSIBLE PERSON
a. REPORT	b. ABSTRACT	c. THIS PAGE			Dr. Andrew G. Godfrey
U	U	U	UU	73	19b. TELEPHONE NUMBER *(include area code)* (540) 557–1900

Standard Form 298 (Rev. 8–98)
Prescribed by ANSI Std. Z39.18

STTR AF00-T019 Phase II Final Report
Contract No. F49620-02-C-0048
"SYSTEMATIC INVESTIGATION OF BLUFF-BODY
COMBUSTION INSTABILITY"

Principal Investigator:
Andrew G. Godfrey
AeroSoft, Inc.
1872 Pratt Drive, Suite 1275
Blacksburg, VA 24060

Contract Manager:
Lt. Col. Juan Vasquez, AFRL/AFOSR
4015 Wilson Blvd., Room 713
Arlington, VA 22203

July 23, 2002 – October 22, 2004

Contents

List of Figures

Chapter 1

Overview

1.1 Identification of the Problem

After several decades of work, many unresolved issues remain associated with the generation and control of thermoacoustic combustion instabilities in full-scale combustors. Academia has been working on theoretical, numerical, and experimental aspects of combustion instabiltiy which can be transferred to immediate relevance for design engineers in the combustion industry. From the industrial perspective, an urgent need exists for the development of usable models which can predict, at some defined level of certainty, the potential occurrence of combustion instabilities over the entire operating range of input conditions. Because of the nonlinear, coupled, and very complex nature of the physical processes underlying the instabilities, it is highly desirable that these models be developed using simplified, reduced-order structures. Modeling efforts of this type are ongoing. However, the complexity of the unstable thermoacoustic dynamics may also be addressed through the use of more detailed CFD modeling approaches. This approach has the distinct advantage of providing field information which is especially important in active combustion control (ACC).

Advances in CFD software and related hardware have greatly enhanced the prospects for physics-based modeling of chemically reacting flows. Naturally, as the CFD field matures, its influence on design and analysis in advanced aerospace applications becomes more prevalent. For example, the structured flow package, $\mathcal{GASP}$, licensed by AeroSoft, provides a wide variety of user-controlled options for modeling subsonic, transonic, supersonic and hypersonic flows. These include an extensive chemistry database containing species, reactions and models of interest, options for frozen or non-equilibrium chemistry, and multiple options for thermodynamics and turbulence modeling.

From experience with augmentors, we know that bluff-body burners equipped with multiple fuel injectors can increase fuel/air mixing and, therefore, could be used effectively in the main burner as well. However, thermoacoustic instabilities can cause structural damage when acoustic pressure fluctuations couple with unsteady heat release from combustion. Light-weight active control systems, which focus on the mixing behind these bluff-body burners, can alter the feedback mechanism and reduce the thermo-acoustic instability. Defining such a system requires a tool for determining generic combustor characteristics which inspires for our approach.

We make a concerted effort to develop and test an unsteady, sensitivity tool using high-
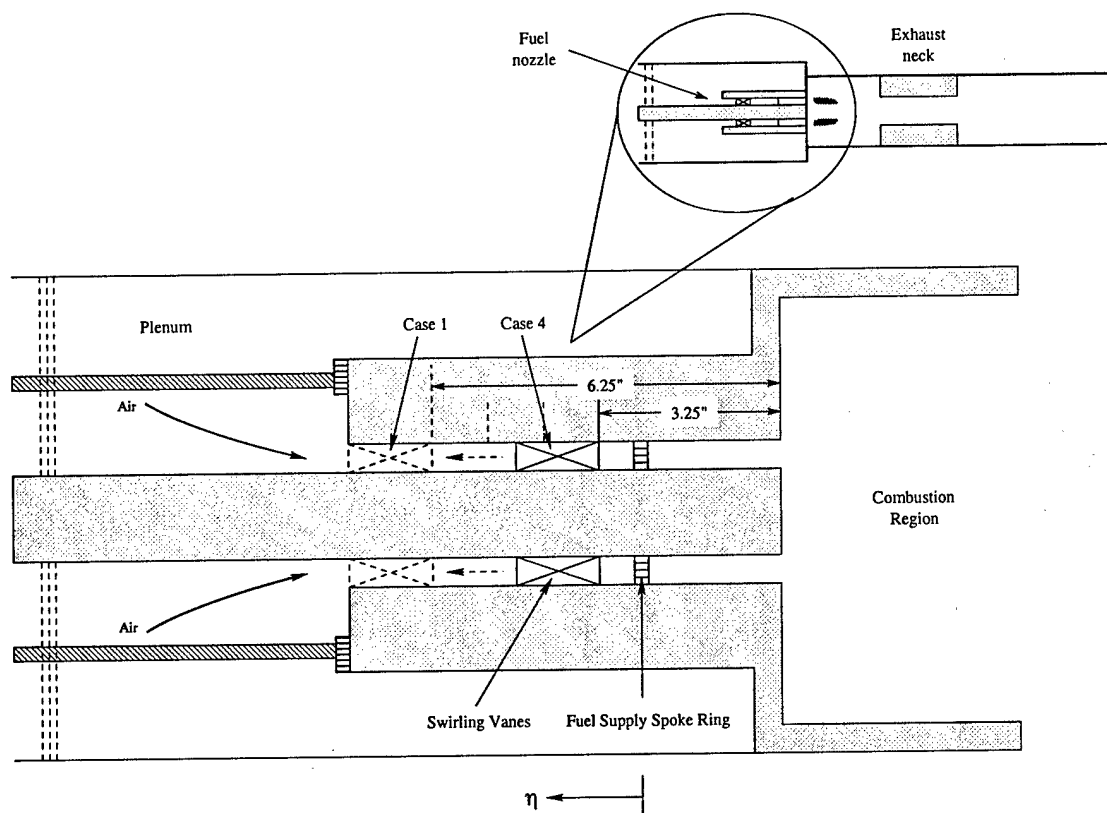
Figure 1.1: Fuel nozzle showing the range of positions for the swirling vanes.

order computational simulations, experimental results for verification/validation, and optimal control laws to control combustion flow fields susceptible to thermo-acoustic instabilities.

1.2   Technical Problem Addressed in Phase I

The Phase I effort addressed the computational problem of modeling steady and unsteady combustion in a generic dump combustor with swirl (see Figure 1.1). We studied two components of the combustor computationally: (1) the swirling air/methane mixing inside the fuel nozzle, and (2) the response in the combustion region to a time-dependent velocity profile. We were interested in the sensitivity of the flow field with respect to the axial position of the swirling vanes and to the axial jet velocity. We solved the flow equations using AeroSoft's $\mathcal{GASP}$ flow solver and the sensitivity equations using the Sensitivity Equation Method (SEM) incorporated into AeroSoft's $\mathcal{SENSE}$ software. We identified an effectivean elementary chemical-kinetics model which uses 32 reactions and 12 species. The project, however, did not solve the unsteady sensitivity equations, which inspires part of the Phase II plan.

1.3   Relationship to Phase II

The selection of a chemistry model and the implementation of that model into the $\mathcal{GASP}$ flow solver and $\mathcal{SENSE}$ sensitivity code was the main accomplishment of the Phase I. We uncovered several computational issues to improve including tight-coupling of the sensitivity solver into the flow solver for true unsteady sensitivities and the incorporation of methods to relieve the stiffness of chemically reacting, time-dependent problems. Additionally, a coupling mechanism must exist between acoustic and heat-release perturbations to accurately model combustion instabilities. Through experience and research of related combustion literature, we emphasize the importance of internal-flow boundary conditions upon the self-excitation of the instability. These are issues which we address in Phase II.

1.4   Project Objectives

The overall goal of this project is to provide a sensitivity-analysis tool for the control of heat-release rate distribution in aeroengine combustors with emphasis on bluff-body type flame-holders. A bluff body serves as the anchoring mechanism and we are interested in the best way to introduce fuel into the combusting flow. This report documents the objectives, work carried out and results obtained during the Phase II project. To achieve the Phase II goals, the following technical objectives are given below:

1. Using parametric, scaled experiments on a 2-D, bluff-body combustor, we obtain a complete characterization of the steady and unsteady conditions. Additionally, a parametric study of the combustion performance will be conducted under open-loop control. Data from these experiments will help test the computational tool.

2. Implement a variety of computational elements for simulating combustion instabilities: (1) time-accurate numerics which address chemically reacting flows, (2) a two-parameter coupling mechanism between acoustic and convective disturbances, and (3) non-reflective boundary conditions to remove numerical noise.

3. Combine developed sensitivity technologies with a commercial flow-solver package to compute sensitivities to actuator parameters. Truly unsteady sensitivities can only be obtained by tightly coupling the flow and sensitivity solvers. Therefore, we couple the two and beneficially enhance the commercial appeal of $\mathcal{GASP}$ in the process.

4. A distributed-parameter control model has been formulated to qualitatively capture thermo-acoustic instability features in a combustion process. Tools for numerical simulation and stability analysis have been developed and demonstrated. Feedback stabilization has been investigated through two optimal control problems.

Chapter 2

Phase II Work and Reults

2.1 Experimental Study of Bluff-Body Combustor

Conceptual Design

In the case of bluff-body stabilized combustion, strong coupling between acoustic and shear-layer instabilities is expected. This will manifest itself in the shedding of large-scale structures, which are typically straddled by the flame/combustion zone. In the conceptual stage, we used simple, cold-flow CFD simulations to obtain an approximation of these flow structures. The geometrical configuration was that of the coaxial bluff-body combustor shown schematically in Figure 2.1. This calculation assumes two-dimensional flow and is modeled using the RNG $K-\epsilon$ model with second-order accuracy in time and space.

The most important piece of information from the calculation is the frequency content of the flow. A time series of vorticity magnitude is shown in Figure 2.2. We can clearly see the shedding of alternating vortices. The frequency contents of the turbulent flow-field was probed (from numerical data) at six locations downstream of the bluff body. A magnification of the spectra is shown in Figure 2.3 which indicates an existence of both odd and even harmonics for the lower inlet-velocity case (*i.e.*, 15 m/s). For the higher velocity case (30 m/s), only the even harmonics exist. In both cases (15 m/s and 30 m/s) the fundamental vortex shedding frequency corresponds to a Strouhal number of 0.3. Note that from Figure 2.2, the time taken for one vortex to shed is approximately $8 \times 10^{-3} s$, which corresponds to a frequency of 125 Hz. The frequency calculated by FFT is 120 Hz (for the 15 m/s case) which corresponds to a shedding time of approximately $8.33 \times 10^{-3} s$.

Preliminary Design

With the cold-flow calculations complete, we moved to design a combustor for acoustic frequencies in the range of 50-500 Hz. Because we wish to excite different frequencies, the design calls for an ability to change the combustor's acoustic characteristics by either changing the bluff-body mounting arm or adding downstream sections to the test facility. Initial concepts of mounting the bluff-body on an arm guided by slip bearings was discounted because of cost and construction complications. Maximum optical access of the test section is desired which includes ports for upstream and downstream acoustic excitation.

The preliminary design of the test rig is shown in Figure 2.4. The rig is fully modular
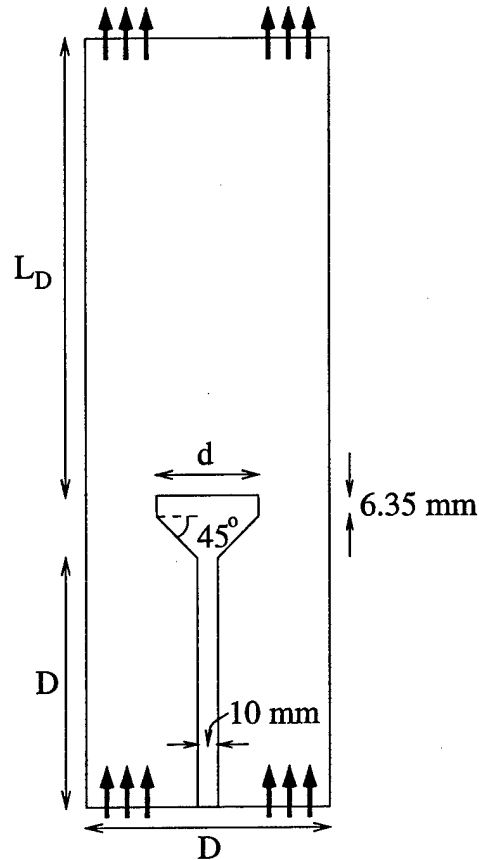
Figure 2.1: Coaxial bluff-body combustor geometry used in the CFD simulation. Dimensions: $D = 76.2\,mm.$, $L_D = 3D$, $d = D/2$.

and comprises flow conditioning, a combustor section and an exhaust mechanism. The rig can be operated in both pre-mixed and diffusion modes. The combustion section has a circular geometry with a diameter of 101.6 mm (4 in) and a length of 508 mm. The flame section is air-cooled and double-walled. Quartz windows are provided on three sides for viewing-access and optical diagnosis. The chamber can be acoustically modified by the addition of downstream sections. A back-pressure valve in the exhaust section provides the capability of operating the test rig at elevated pressures. The water-cooled bluff body is shown in Figure 2.5. The disc measures 50.8 mm in diameter and the body if fitted with one axial-injection hole and four radial-injection holes, each located 90° apart. Each of the five jets has an independent fuel supply and control.

   A second CFD investigation was performed for the preliminary combustor under hot-flow conditions. Parametric studies were conducted with mean combustor inlet velocities of 30 and 15 m/s to determine the size and shape of the bluff body and size of the injection holes. From the initial cold-flow study, an incoming inlet velocity of 15 m/s vortex-shedding frequency of 120 Hz (corresponding to a Strouhal number of 0.3). Reacting flow was simulated for the geometry shown in Figure 2.6. Three injection holes were included in the bluff body geometry to account for the methane fuel injection from the bluff body. Two radial holes on

$t = 5 \times 10^{-3}\,s$ $t = 6 \times 10^{-3}\,s$ $t = 7 \times 10^{-3}\,s$

$t = 8 \times 10^{-3}\,s$ $t = 9 \times 10^{-3}\,s$

Figure 2.2: Vorticity magnitude contours ($U_{inlet} = 15\,m/s$).
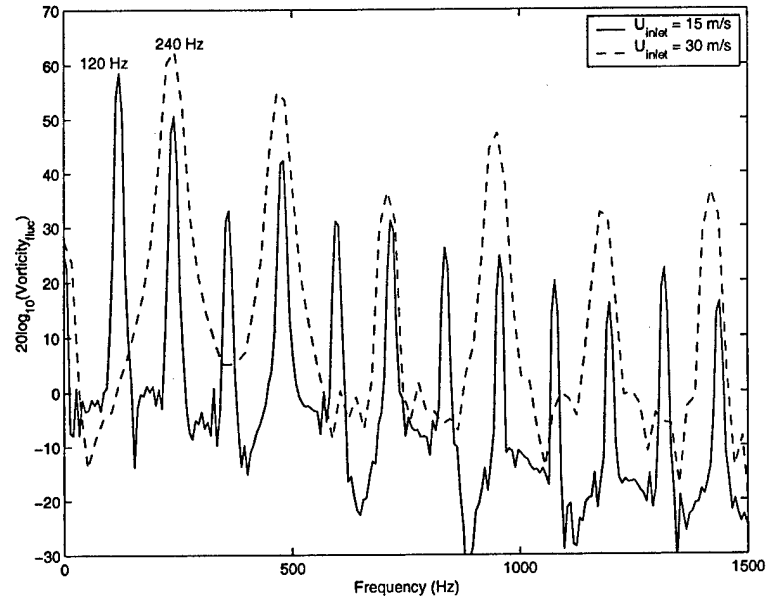
Figure 2.3: Power spectrum plot of vorticity magnitude (Pt11; $U_{inlet} = 15\,m/s$ and $30\,m/s$).
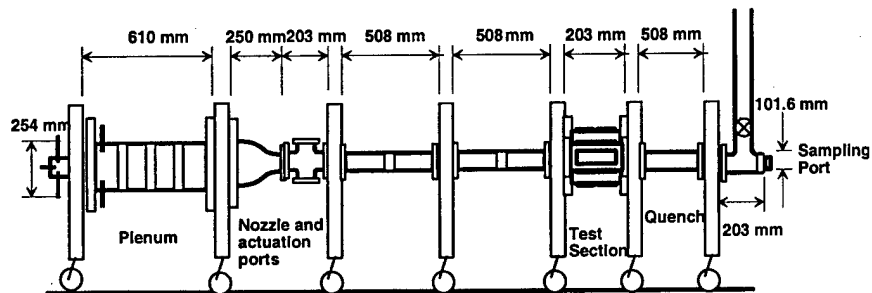
Figure 2.4: Schematic of the combustor experimental set-up.
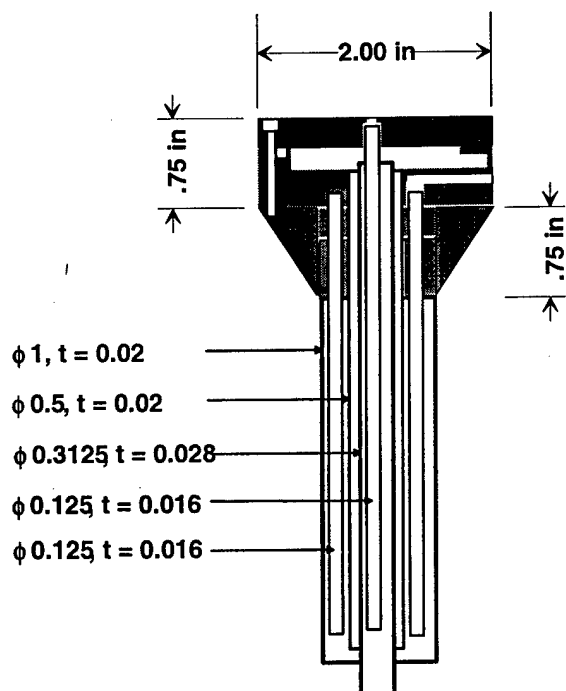
Figure 2.5: Schematic of the water-cooled bluff body.

the top/bottom of the bluff body and one axial hole are considered.

A large eddy simulation (LES) of the reacting flow was carried out using the localized dynamic sub-grid model (LDKM) and a 15-step reduced reaction mechanism for methane-air premixed combustion (where the equivalence ratio was $\phi = 0.5$). The calculations predict that the flame in anchored by the bluff body and that no vortex shedding was present. Even though combustion tends to homogenize the vortex shedding process, these results were considered preliminary and therefore a final conclusion could not be drawn concerning vortex shedding.

With preliminary design work and reacting-flow simulations complete, efforts then focused on the development of an experimental combustion test facility at Virginia Tech. A
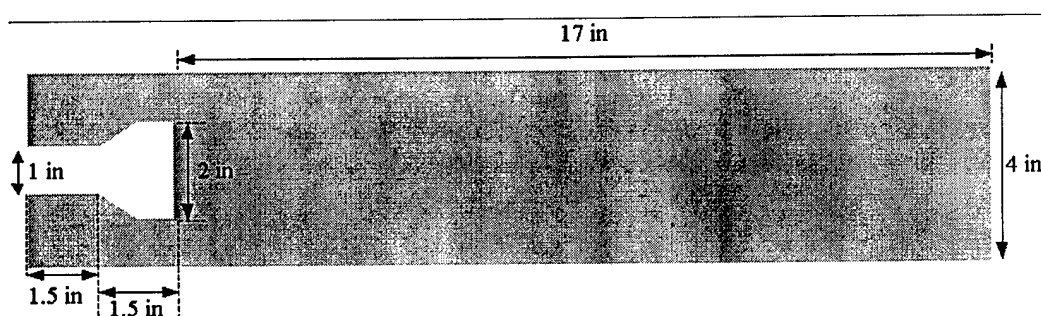
Figure 2.6: Internal geometry for the CFD analysis

Mean Inlet Cross-flow Velocity of Premixed Charge (m/s)	15
Equivalence Ratio	0.5
Cross Flow Density (kg/m3)	1.155
Air Mass Flow Rate (kg/s)	0.138
Air Volume Flow Rate (scfm)	250.458
Fuel Mass Flow Rate (kg/s)	0.004
Fuel Volume Flow Rate (scfm)	13.204
Total Volume Flow Rate in Pre-mixer (scfm)	263.663
Cross Flow Reynolds No	66671.481
Cross flow Velocity at Radial Injection Plane (m/s)	19.914
Injection Diameter (mm)	2
Modulation Mass Flow Rate (kg/s)	10% of the fuel in the cross flow
Modulation Volume Flow Rate (scfm)	1.320
Modulation Jet Velocity (m/s)	126.936
Modulation Jet Reynolds No	18865.844
Thermal Power of the Rig (W)	222117.188

Table 2.1: Combustor rig parametrics.

facility capable of providing 1200 scfm of vitiated airflow at 190 psig (which can be enhanced
to 35 bar maximum) pressure and $1050°F$ temperature was established. On the fuel side,
natural gas supplies at 750 psig was constructed. A desire to automate the operation of
the facility in terms of supervision and running the rig was completed. Detailed engineering
drawings of the combustor test rig (portions of which are shown in Figure 2.7(a) and Fig-
ure 2.7(b)) were completed and sent to Virginia Tech's machining operation for milling and
fabrication.

Design Rig Summary The rig is 187 in. long and can be operated at 5 bar maximum
pressure. The dual-shell combustion section has a circular geometry and is air-cooled. Op-
tical access is provided on three sides for viewing and diagnosis. The chamber can be either
acoustically forced or modified to be self-excited. The water-cooled bluff body has a disc
diameter of 2 in. with one axial and four (90° apart) radial injection holes, each with inde-
pendent fuel supply and control. The main operating parameters of the combustor are given
in Table 2.1.

Combustor Fabrication

The fabrication of the high-pressure combustor rig took place in two locations. The ma-
jority of the parts were fabricated and assembled at the Virginia Tech Mechanical Engi-
neering (ME) Department's Machine Shop. The combustor balance was constructed by a
University contractor.

    At this point, the experimental portion of the project began experiencing set-backs.
When the rig became 65% complete, budget cuts by the state of Virginia began to hamper
progress. The ME portion of the job was done free of charge to the project. However, budget
costs constrained the amount of man power and time that was assigned to the project. Once
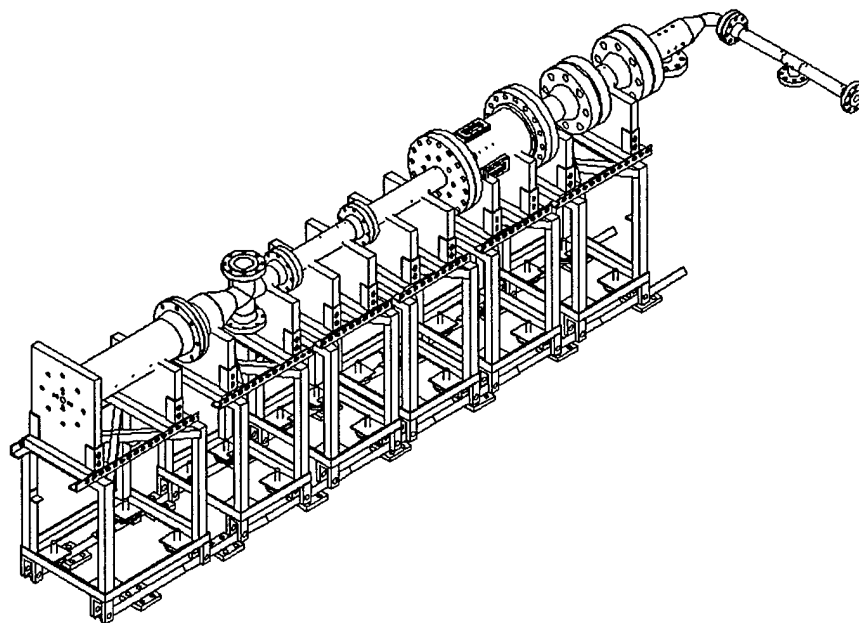
(a) 3-D view of rig.
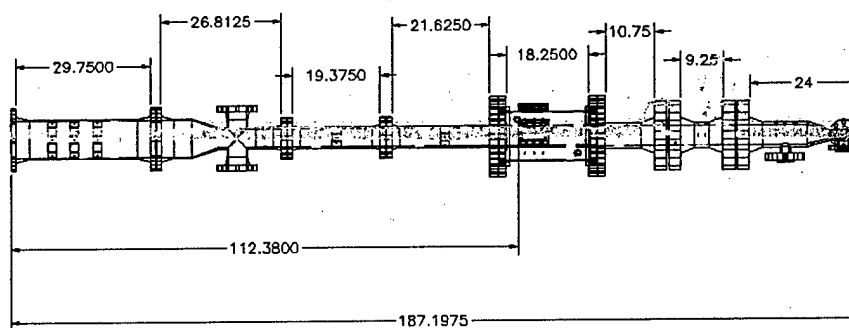
(b) Dimensions of rig.

Figure 2.7: Bluff-body combustor view and dimensions.
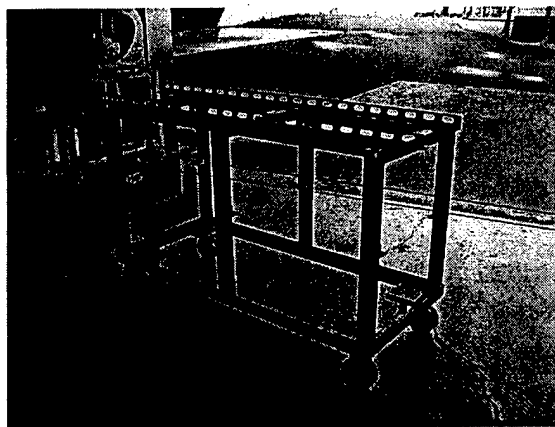
(a) One of four support carts.

(b) Parts of high-pressure combustor section.
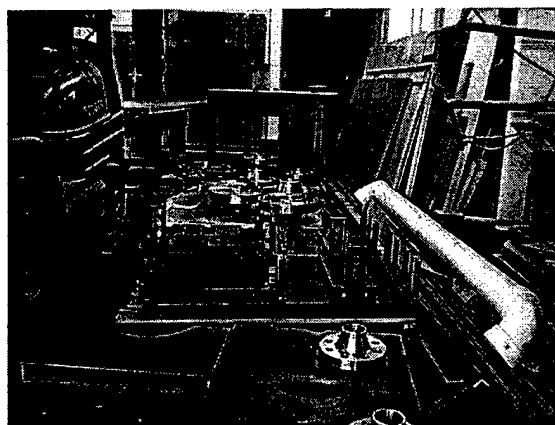
(c) Flow-train support brackets.
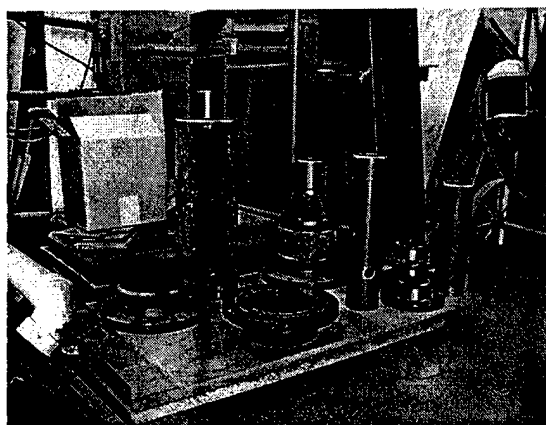
(d) Flow conditioning parts.

Figure 2.8: Current parts of the experimental rig.

the machining activities ended, welding of the large stainless steel flanges commenced by an ASME-certified outfit in Salem, Virginia. Some of the parts are shown in Figure 2.8 and Figure 2.9.

After many delays, assembly of the combustor rig was accomplished (see Figure 2.10 for the assembled combustor rig). The compressed air, fuel and water (for cooling the bluff body and the exhaust gases) feed systems were checked for high-pressure leaks and functionality of the safety system. Work then began on setting up the process-control electronics and wiring.

Combustor Results

Experimental investigations were conducted on the 250 kW natural gas combustor rig, shown in Figure 2.10. Fuel for the pilot flame was supplied to the combustor section through the axial injector on the bluff body (shown in Figure 2.20), while for the main premix
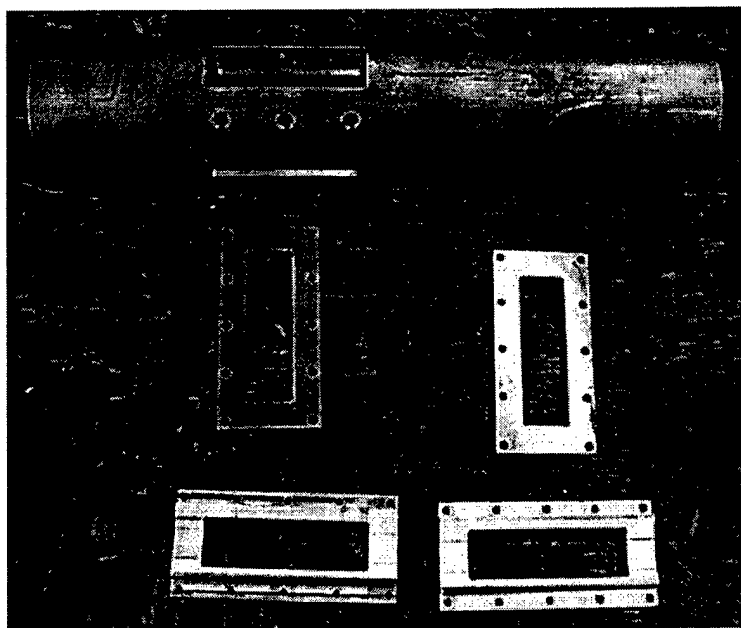
(a) Combustor section and window brackets.
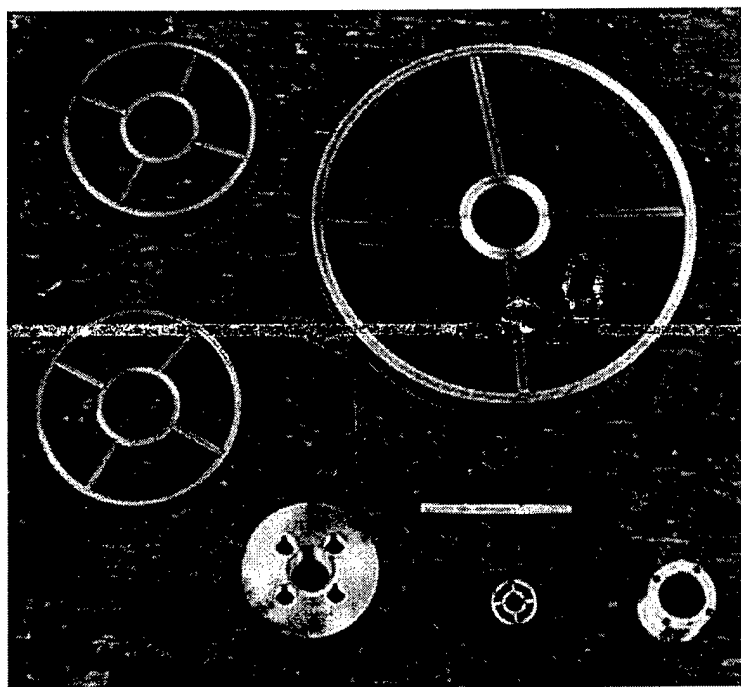
(b) Guide sleeves and screens.

Figure 2.9: Combustor parts.
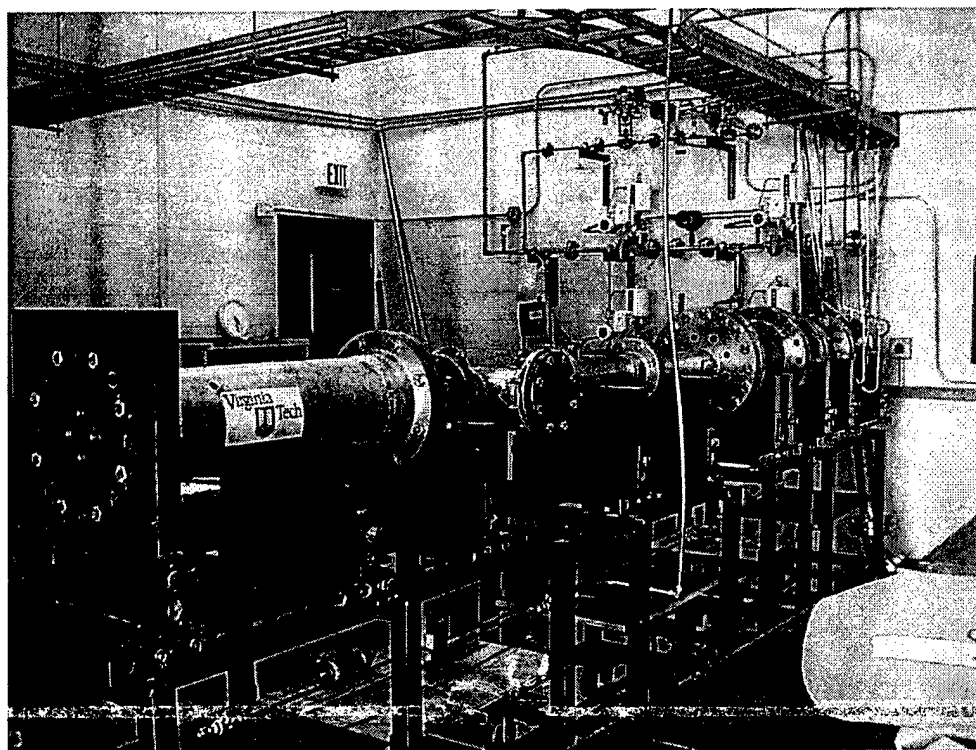
Figure 2.10: Assembled combustor rig.
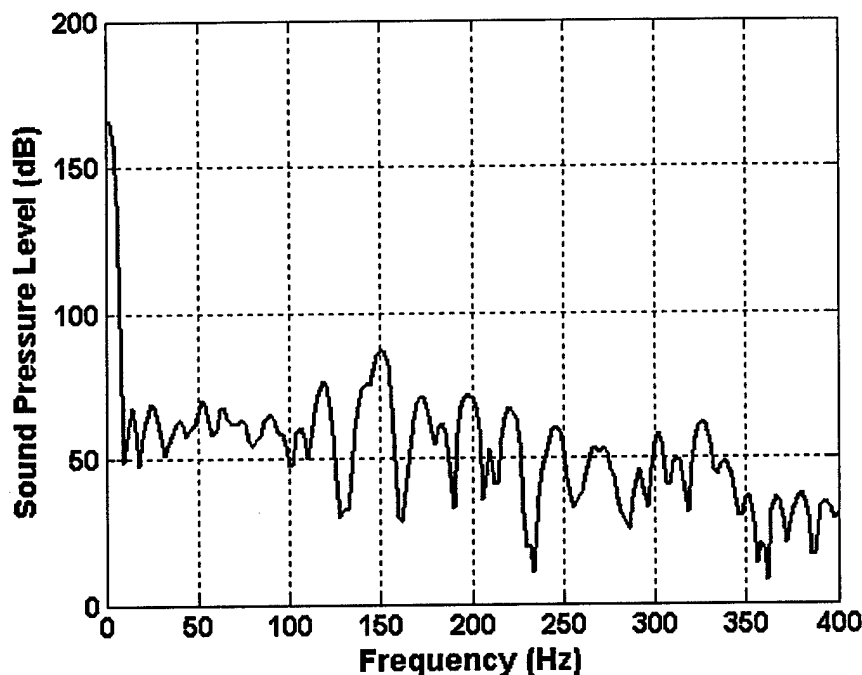
Figure 2.11: Combustor power spectrum under *non-reacting* 156 g/s airflow.

combustion, the fuel and the air were routed through a pre-mixer before it was introduced in the combustor. Flow straighteners were provided along the length of the rig to streamline the flow. Pressure and temperature measurement ports were provided along the length of the rig. Preliminary characterization experiments were performed at atmospheric pressure and temperature conditions.

For these experiments, temperatures and dynamic pressures were measured at 50 mm downstream of the bluff body face. The temperatures recorded represent the centerline flow values. Type B thermocouples were used for the flame area temperature measurements. Dynamic-pressure measurements were recorded using differential pressure transducers from Honeywell Model SX01D. A remote-controlled flame-torch was used to ignite the pilot flame, which in turn ignited the premixed charge. The preliminary results are presented here.

Non-Reacting Flow The acoustic characteristic of the combustor in the presence of 156 g/s (275 scfm) airflow is shown in Figure 2.11. As mentioned earlier, the measurements were made 50 mm downstream of the bluff body. The power spectrum depicts some pronounced energy at 150 Hz, which may be the vortex shedding frequency.

Figure 2.12 shows the acoustic-pressure spectrum for the pilot flame only. A natural gas flow of 0.15 g/s (0.45 scfm) was introduced through the pilot injector for this diffusion burning measurement, while the air-flow was maintained at 156 g/s. The 150 Hz peak can still be observed, however, a more significant low-frequency peak appears at 46 Hz. The flame temperature measured at the centerline and at the same axial location was 1200 K (1700 °F). The corresponding reacting flow image is given in Figure 2.13.
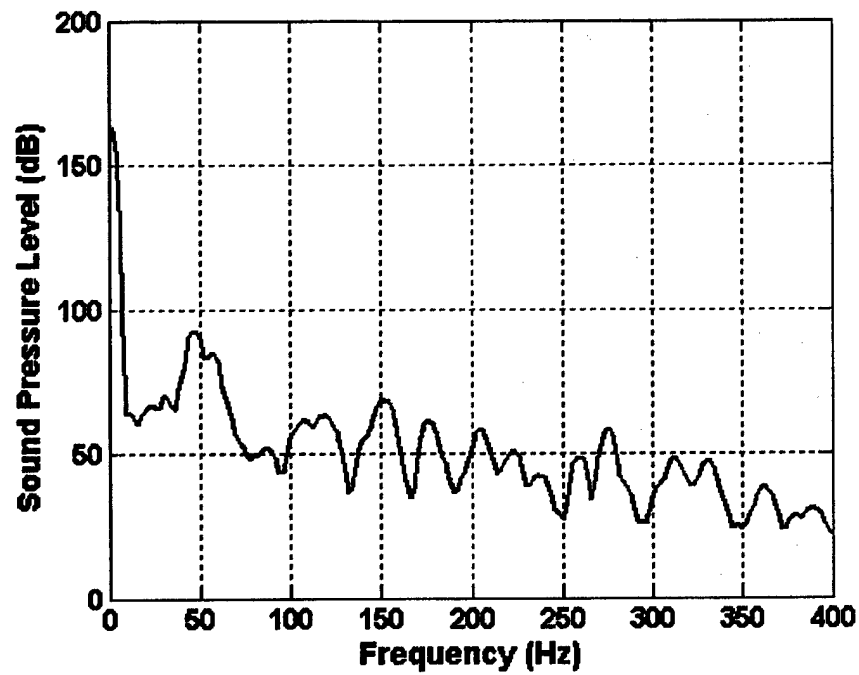
Figure 2.12: Combustor power spectrum for *pilot flame* with 156 g/s air-flow and 0.15 g/s fuel-flow.
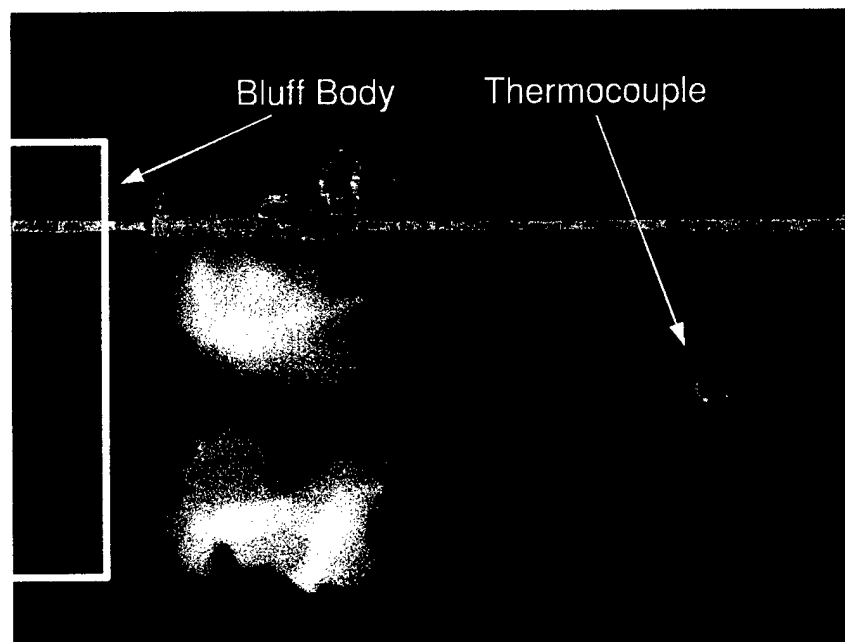
Figure 2.13: Reacting flow field for pilot flame with 156 g/s airflow and 0.15 g/s fuel flow.
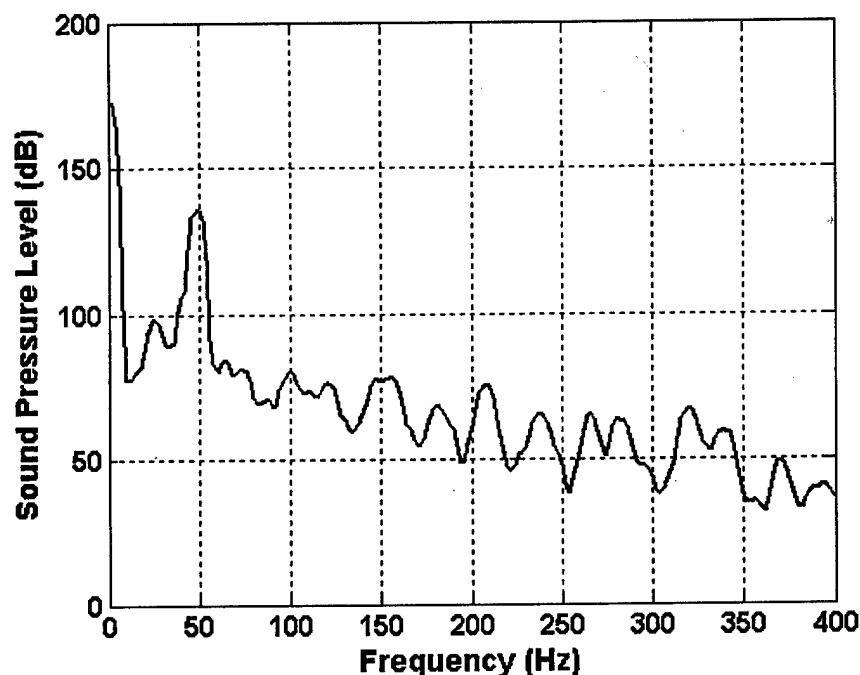
Figure 2.14: Power spectrum with combustion at 0.4 equivalence ratio with pilot flame.

Premixed Charge, $\phi = 0.4$ Premix charge at an equivalence ratio of $\phi = 0.4$, comprising 148 g/s (260 scfm) of air and 3.5 g/s (11 scfm) of natural gas, was then introduced in the combustor. The pilot flame was maintained at the earlier mentioned values. The power spectrum and the corresponding time signal are shown in Figure 2.14 and Figure 2.15, respectively. The low-frequency excitation was more pronounced with a slight shift in frequency to 48 Hz. The flame image for this condition is shown in Figure 2.16. The recorded temperature was 1422 K (2100 °F).

Premixed Charge, $\phi = 0.5$ The equivalence ratio was then increased to $\phi = 0.5$ with air-flow constant and increasing the fuel flow to 4.4 g/s (14 scfm). Once again the pilot flame was maintained. The centerline temperature showed an increase to 1478 K (2200 °F). The power spectrum, shown in Figure 2.17, indicated the disappearance of 150 Hz oscillations, shifting of the low-frequency oscillation to 38 Hz and the appearance of sub-harmonics. This implied a non-linear coupling between the combustor acoustics and the heat-release oscillations. The corresponding time signal and the reacting flow field are shown in Figure 2.18 and Figure 2.19.

During the experiments the pre-mixed flame could not be stabilized without the presence of the pilot diffusion flame. Efforts are in progress to stabilize the flame without the pilot. Once that is achieved, experiments will be conducted to measure acoustic pressures, temperatures, heat release via chemiluminescence and velocity fields via Digital Particle Image Velocimetry (DPIV).
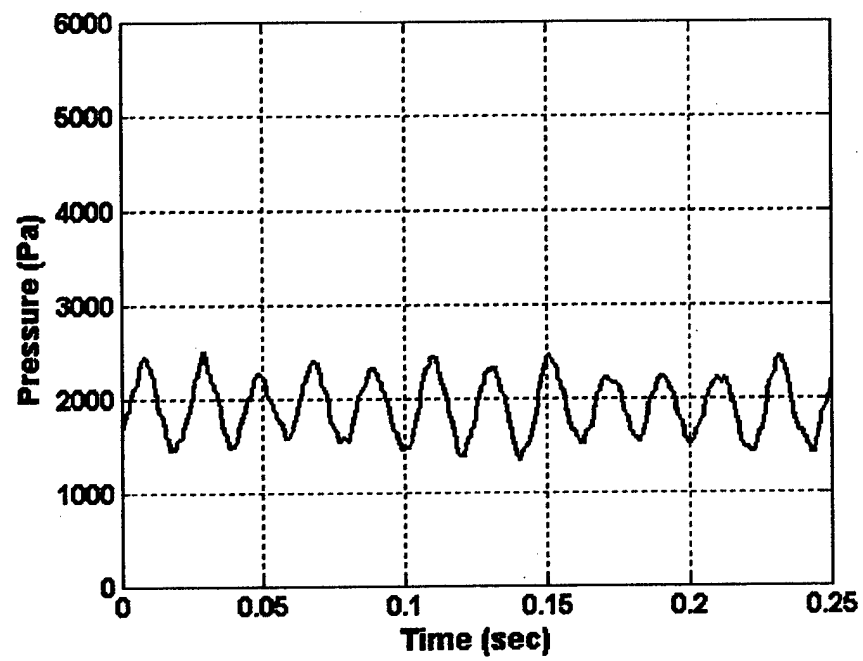
Figure 2.15: Time signal at 0.4 equivalence ratio with pilot flame.
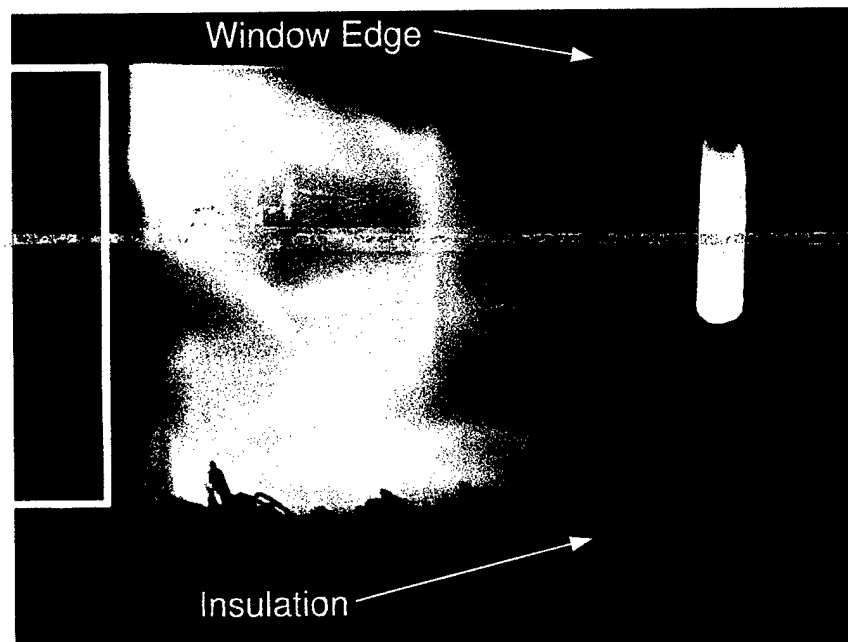
Figure 2.16: Reacting flow image at an equivalence ratio of 0.4.
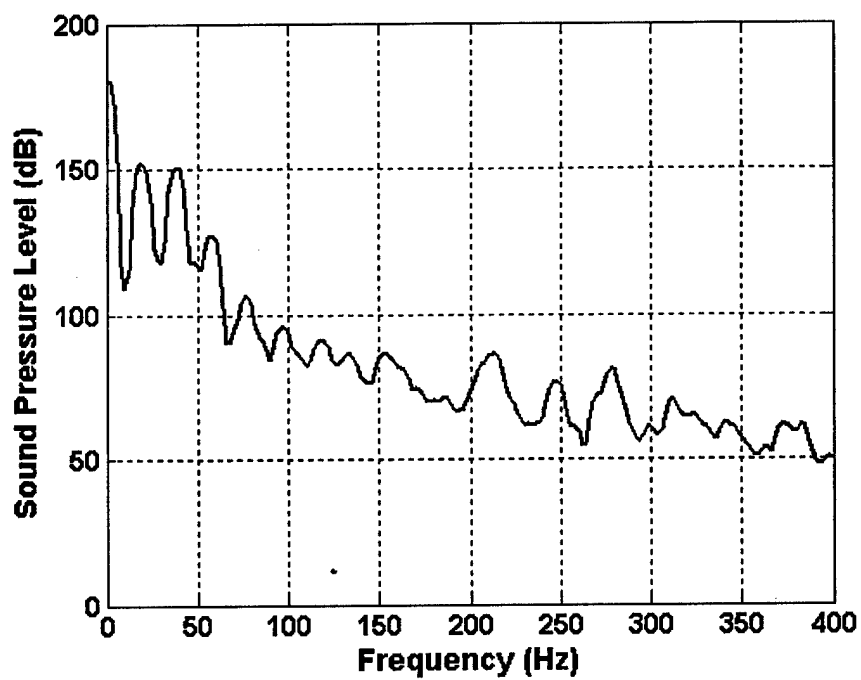
Figure 2.17: Power spectrum with combustion at 0.5 equivalence ratio with pilot flame.
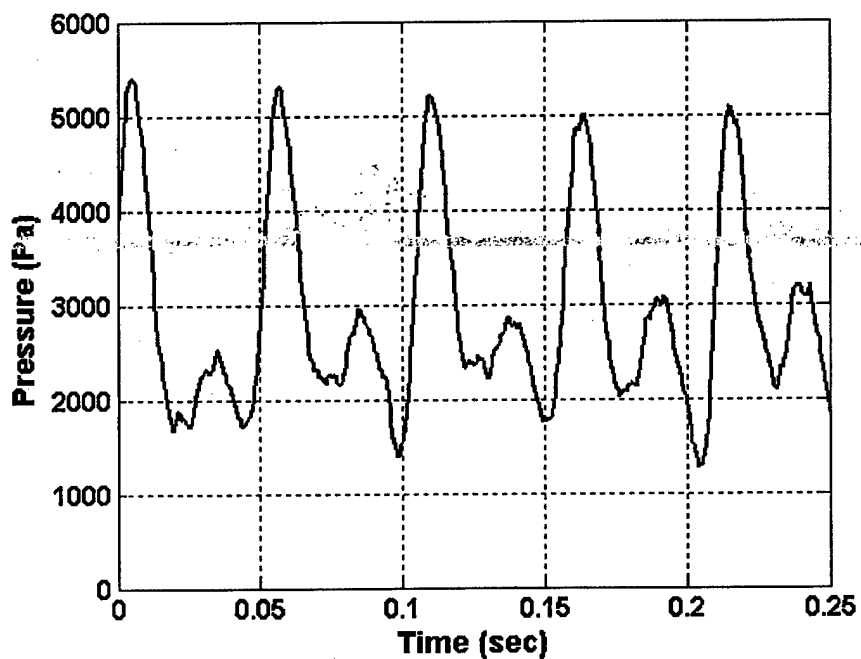
Figure 2.18: Time signal at 0.5 equivalence ratio with pilot flame.
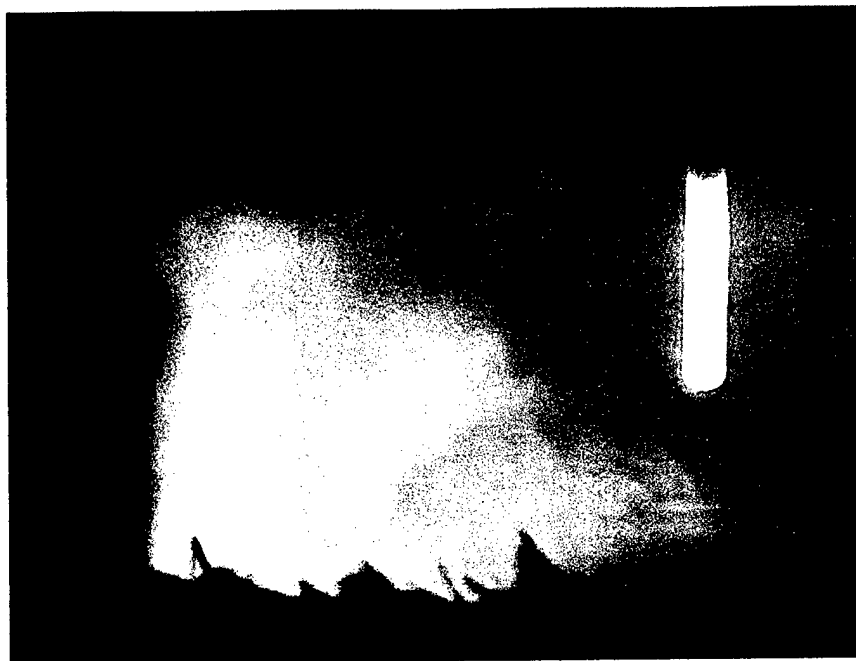
Figure 2.19: Reacting flow image at an equivalence ratio of 0.5.

2.2 Computational Simulation of Combustor

Combustor CFD Calculations

The VACCG combustor consists of a $1\,in$ stem connected to a bluff-body head ($R_i = 1\,in$) enclosed in a pipe ($R_o = 2\,in$). The head is configured to allow for one axial injector ($R = 0.098\,in$) and four radial injectors as shown in Figure 2.20. Each injector is configured with an independent fuel-supply and modulation-control. The radial injectors are spaced at $90°$ intervals and located $0.5\,in$ upstream of the bluff-body base. The upstream conditions are as follows

$$\rho_{N_2} = 0.897493\,kg/m^3$$
$$\rho_{O_2} = 0.272515\,kg/m^3$$
$$\rho_{CH_4} = 0.034156\,kg/m^3$$
$$u = 16\,m/s$$
$$p = 93793.5\,N/m^2.$$

The above conditions correspond to an equivalence ratio of $\phi = 0.5$ and $M \approx 0.05$.

In modeling this flow field, we utilize the methane/air, chemical-kinetics model of Bowman and Seery [1] Bowman and Seery's model assumes a gaseous fluid composed of twelve species (N_2, O_2, CH_4, CO_2, CO, H_2O, H_2, H, OH, O, CH_3 and HCO) and coupled together by 32 elementary reactions. The model proved to be more robust than the global mechanisms tried during the Phase I project. We continue to use the Bowman/Seery model for the Phase II calculations and simulate steady flow through the combustor both with and
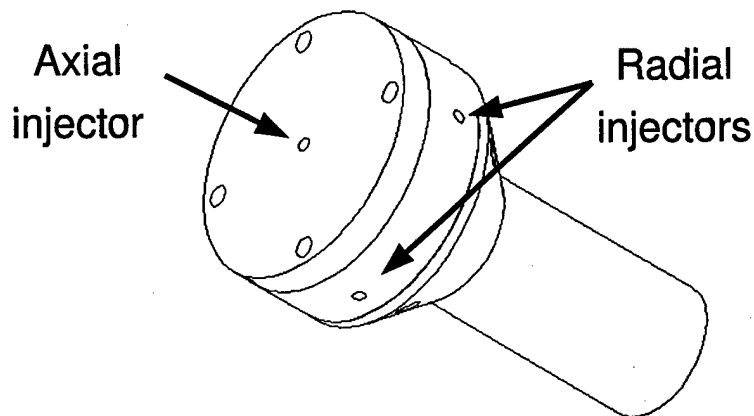
Figure 2.20: Water-cooled bluff-body and stem showing one axial injector (along the singular axis) and two (of four) radial injectors. Note, the four larger holes in the base region are screws.

without axial injection. Chemical reactions are assumed to advance at a finite rate. This is generally much less stiff than assuming equilibrium flow, where reaction-rate coefficients are numerically infinite (*e.g.*, $\sim 10^{15}$).

A Spalart-Allmaras [2] one-equation turbulence model is selected with a third-order, upwind-biased spatial discretization. The domain is discretized with two zones of dimensions 129×41 and 161×85, respectively. Thermodynamics is modeled by assuming equilibrium translation and rotation – that is, the vibrational contribution to internal energy, which is important at much higher temperatures, is neglected. A thin-layer approximation is made in the viscous formulation; cross derivatives are generally important for much lower Reynolds-number flows and require a much higher mesh density than is practical for the duration and resources of this contract. Convergence to a steady state is assumed when mass-fraction contours remain unchanged.

Contours of the steady, pre-mixed simulation without injection are shown in Figure 2.21. Burning gases are stabilized in the re-circulation region of the bluff body. The temperature ranges from $264.8\,K$ to $2623\,K$ and OH mass-fraction is largest (0.99%) near the base. The simulation assumes an axi-symmetric centerline, which is consistent with the observation that chemistry reduces/eliminates the oscillatory shedding of vortices. Note, however, the core flow of burned gases do not spread towards the outer casing wall.

With pure methane injected axially at $132\,m/s$, the temperature and OH mass-fraction contours are shown in Figure 2.22. The density of the methane is $\rho_{CH_4} = 0.648\,kg/m^3$. The peak temperature increases to $2811\,K$ and the peak OH mass fraction is 0.11%. The axial injector significantly changes the OH mass fraction along the singular axis. Contours of the x-component of velocity and CH_3 mass fraction are given in Figure 2.23. Centerline data and profile data are given in Figure 2.24.

3-D, Steady Combustor Calculation

In addition to the two-dimensional combustion cases, we investigated a flow-field simulation iwth all injectors operating. This is a three-dimensional flow field which we have modeled
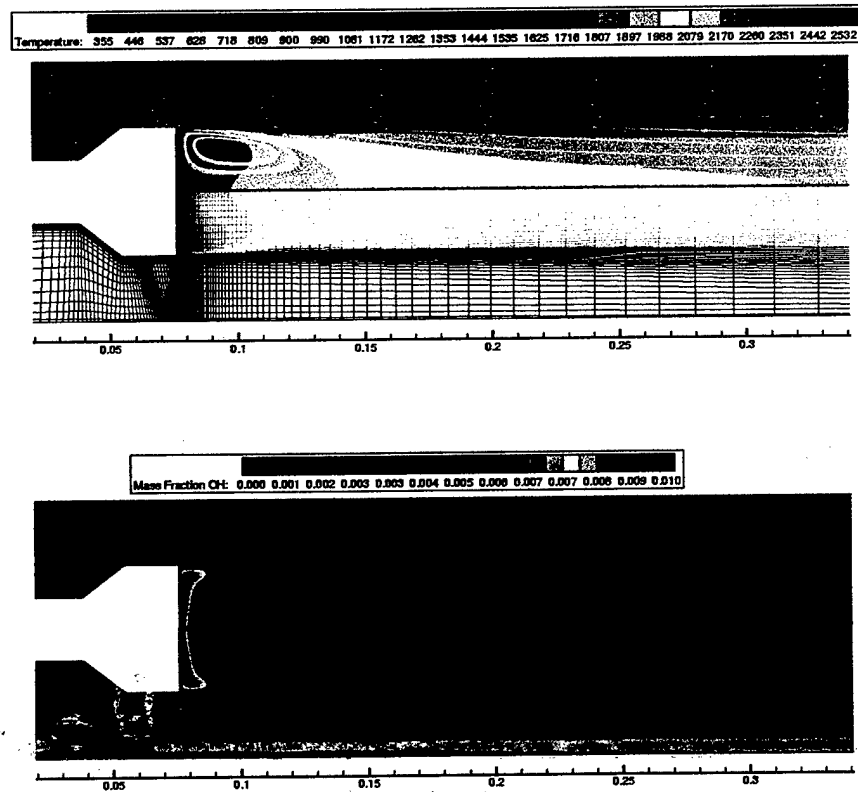
Figure 2.21: Axi-symmetric VACCG combustor *without* injection. Temperature contours, streamlines and grid lines (top) and *OH* flooded mass-fraction contours (bottom).
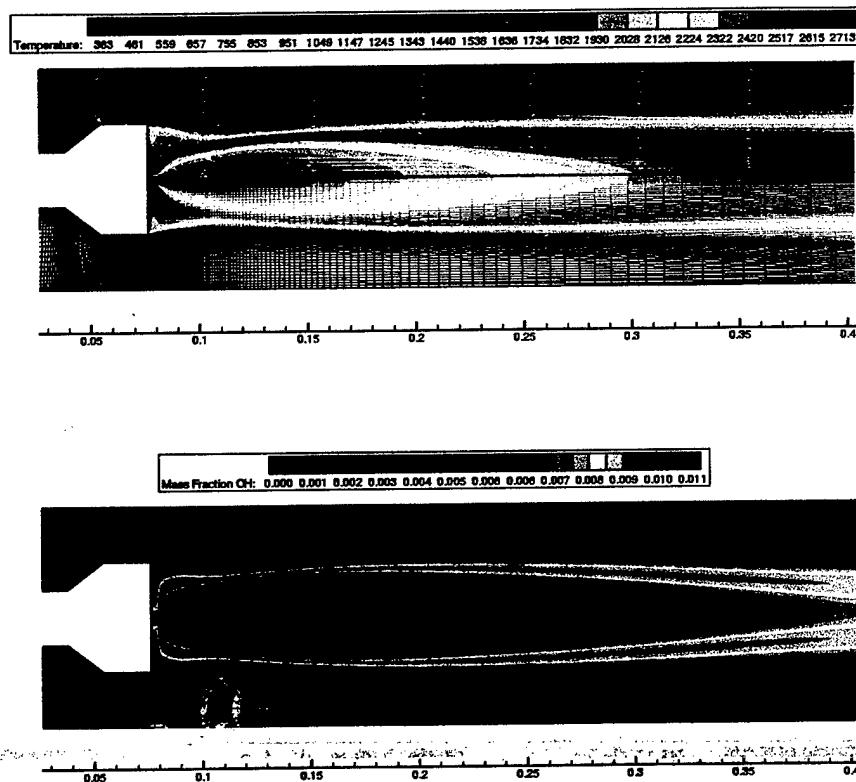
Figure 2.22: Axi-symmetric VACCG combustor with *axial* injection normal to bluff-body base. Temperature constours, streamlines and grid lines (top) and OH flooded mass-fraction contours (bottom).
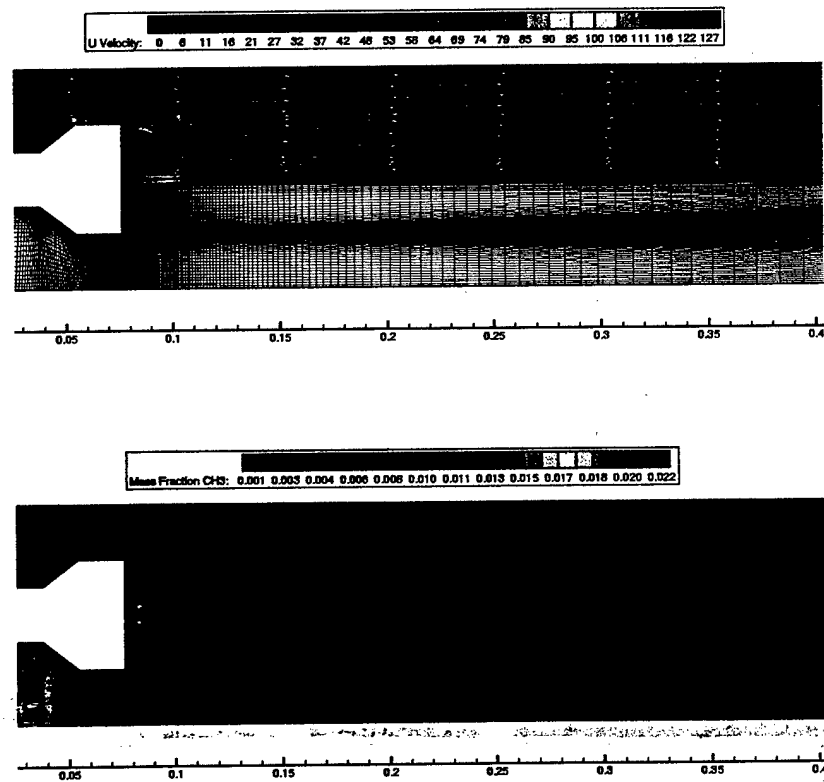
Figure 2.23: Contours of the x-component of velocity and CH_3 mass fraction for the axial-injector VACCG combustor.
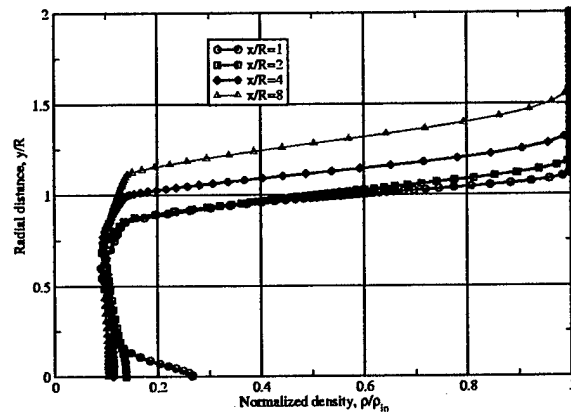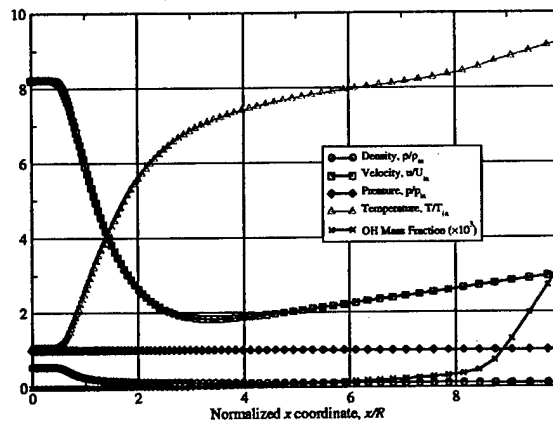
(b) Density profiles.
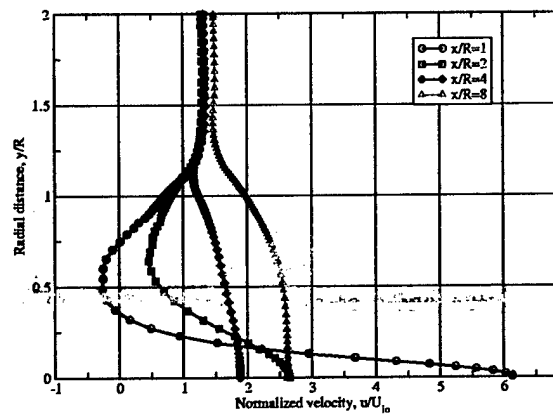
(c) Velocity profiles.
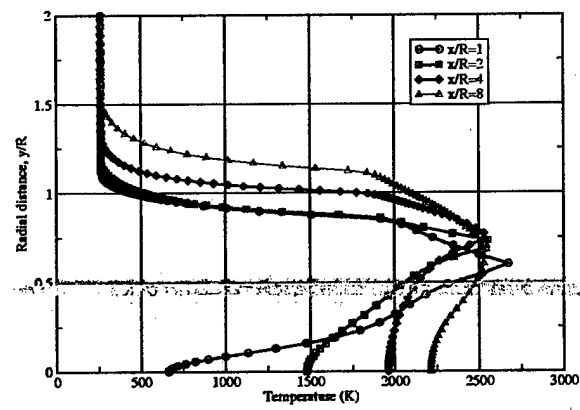
(d) Temperature profiles.

Figure 2.24: Centerline and profile data for axial-injector combustor.
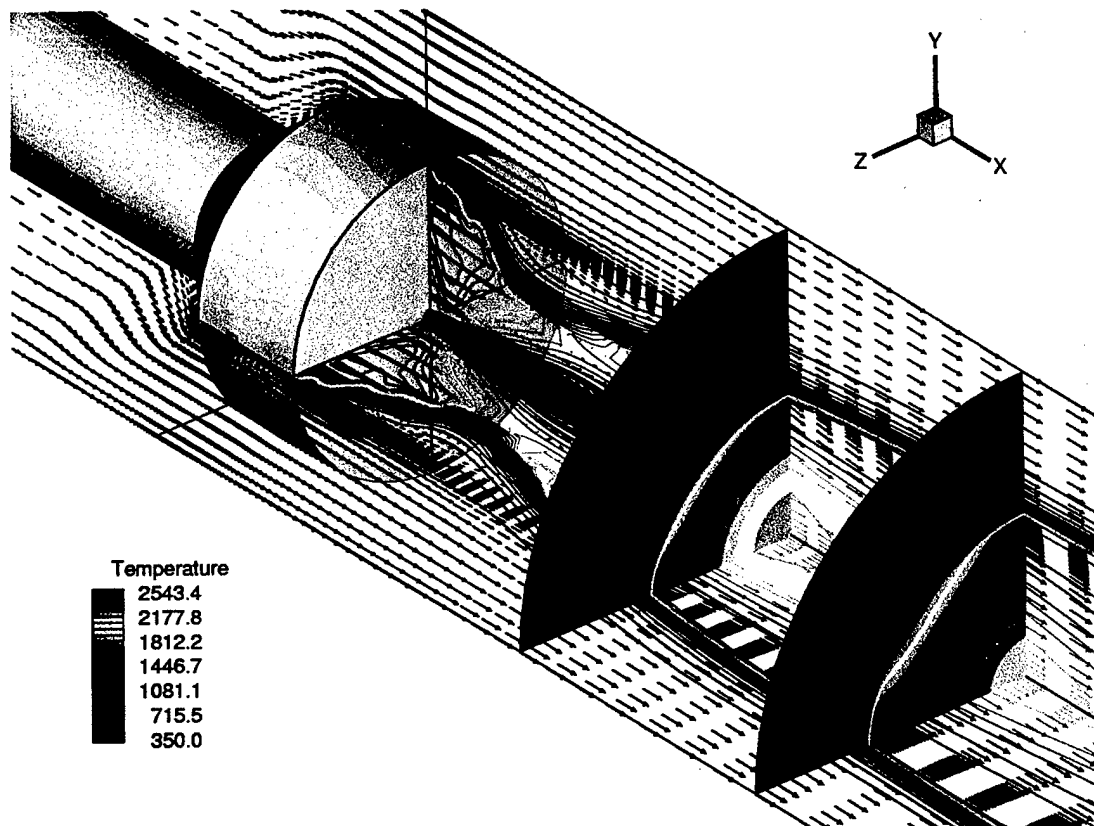
Figure 2.25: Temperature field for the five-injector, three-dimensional VACCG combustor.

as symmetric in the four, azimuthal quadrants. Two zones of sizes $129 \times 41 \times 33$ and $161 \times 85 \times 33$ (593920 cells) are used. Temperature contours and velocity vectors are shown in Figure 2.25 for the case of all five injectors (one axial, four radial). Methane with a density of $0.648\,kg/m^3$ is injected through the five injection holes at equal speed of $26.46\,m/s$. This corresponds to a mass-flow rate of $\dot{m} = 4.21 \times 10^{-4}\,kg/m^3$ which is 10% of the methane mass-flow at the inflow. OH and CH_3 mass-fraction contours are given in Figure 2.26 and Figure 2.27, respectively. Contours of x-component of velocity and stream-traces are shown in Figure 2.28. Centerline and profile data is shown in Figure 2.29. Comparing with the two-dimensional simulations (see Figure 2.24), combustion occurs much closer to the bluff-body base for the three-dimensional simulation. This is caused by the lower injection velocity (26.46 versus $132\,m/s$) in the 3-D case. Peak temperatures reach approximately $2500\,K$ in both cases.

2-D, Unsteady Combustor Calculation

An unsteady, axi-symmetric simulation of pre-mized methane/air flow has been completed using a one-equation Spalart-Allmaras model. A steady-state solution has been used as an initial condition for the unsteady simulation (second-order-accurate in time). The simulation has been run to $T = 45ms$ using a time step of $\Delta t = 5 \times 10^{-7}\,sec$. Snap-shots of the temperature field are shown in Figure 2.30. After $t = 17.5ms$, the unsteady flow structure
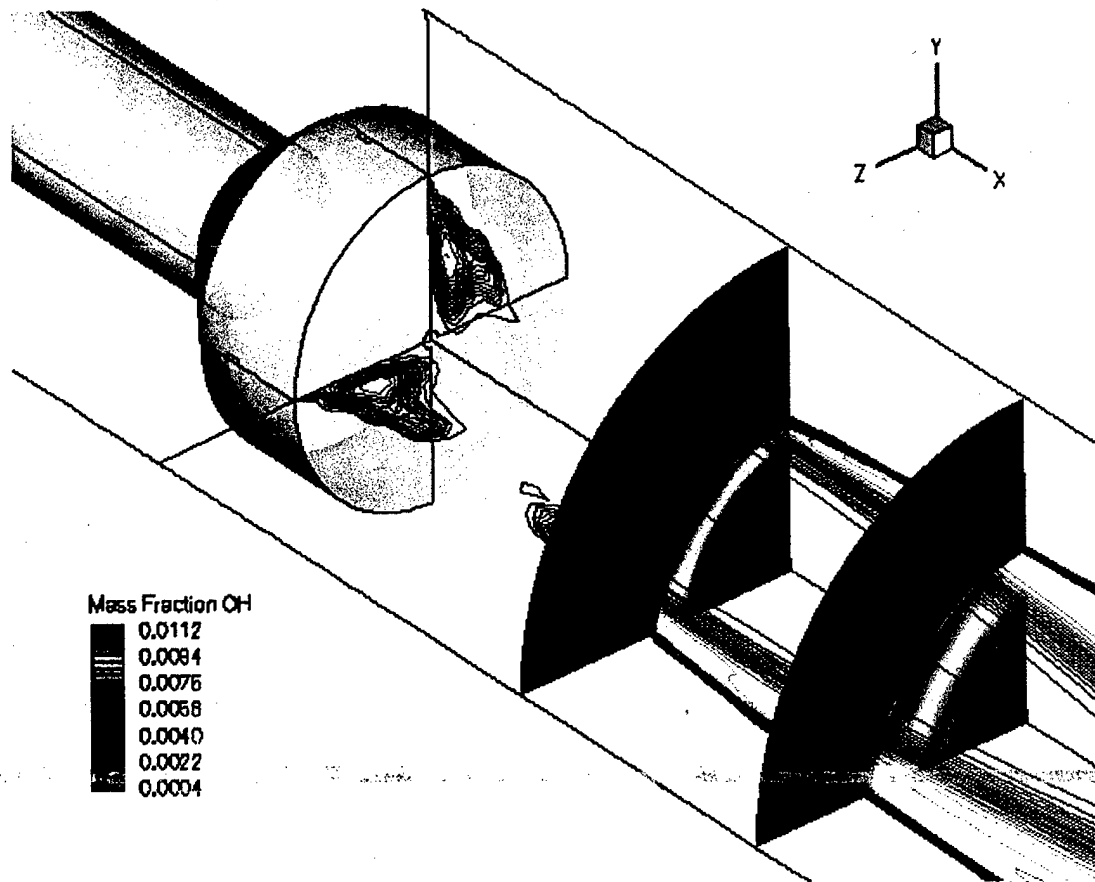
Figure 2.26: *OH* mass-fraction field for the five-injector, three-dimensional VACCG combustor.

Mass Fraction CH3

- 0.0118
- 0.0099
- 0.0080
- 0.0061
- 0.0042
- 0.0024
- 0.0005
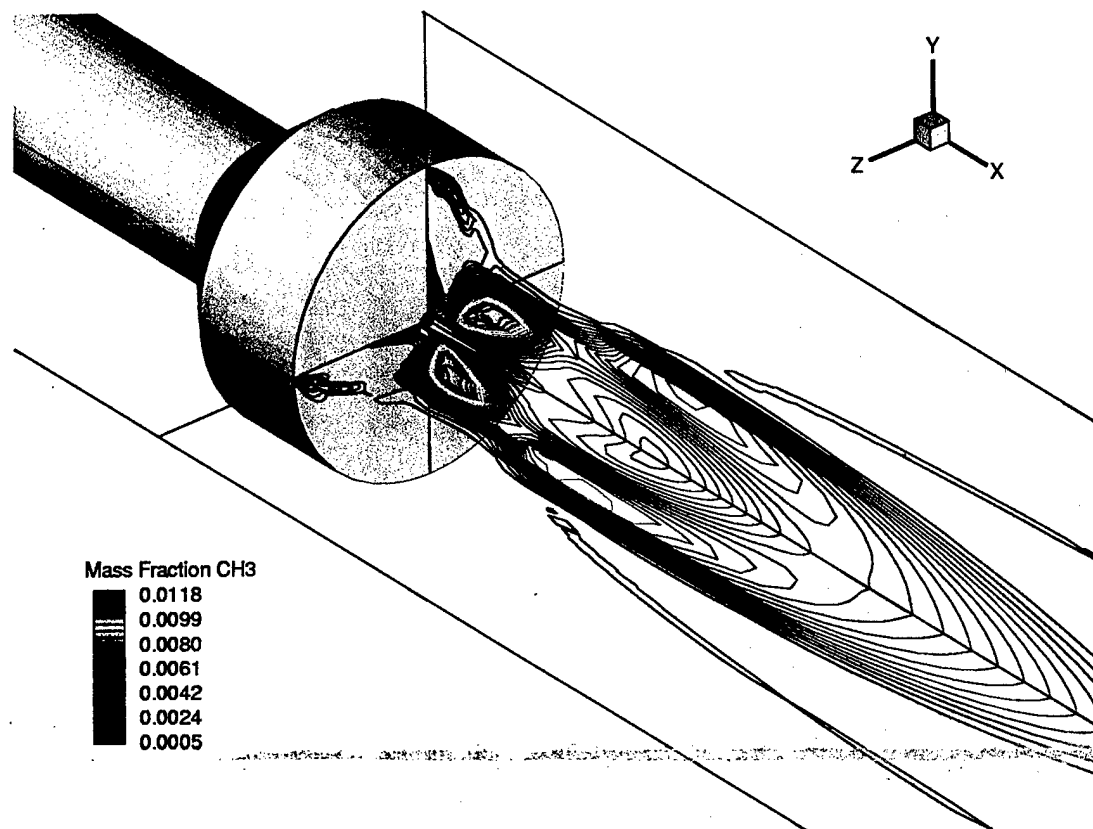
Figure 2.27: CH_3 mass-fraction field for the five-injector, three-dimensional VACCG combustor.
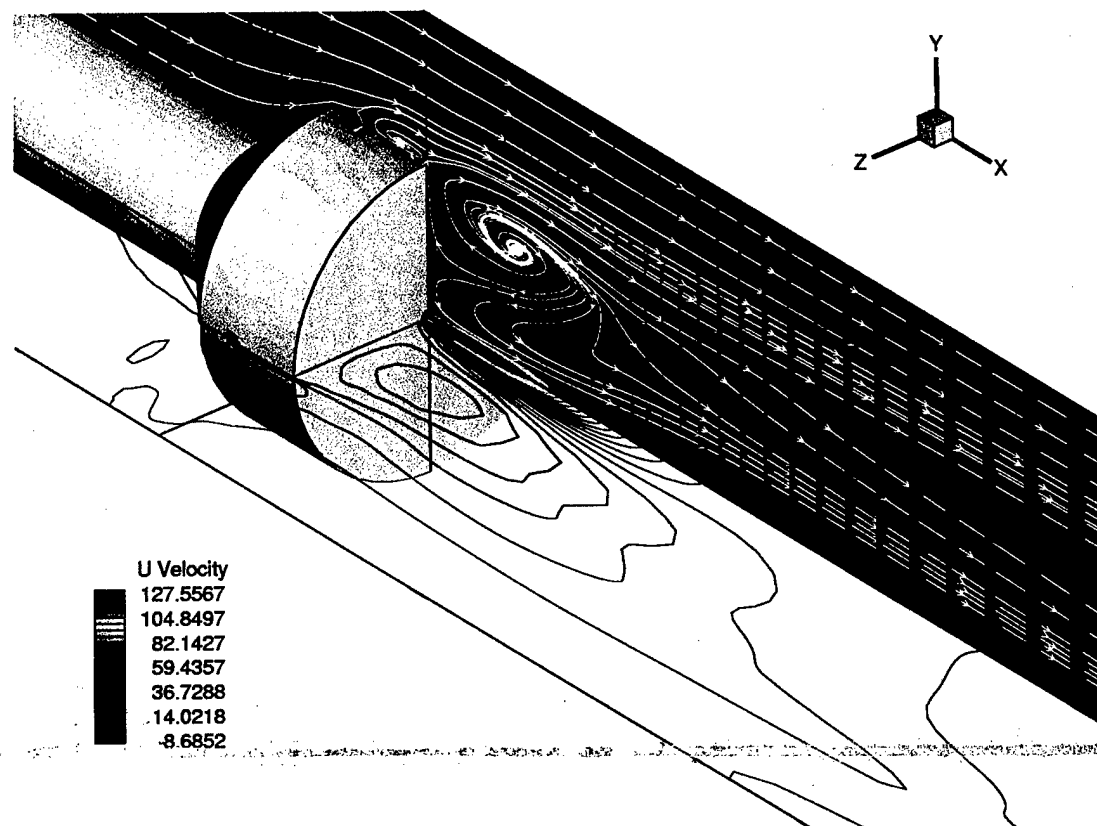
Figure 2.28: Contours of the x-component of velocity for the five-injector, three-dimensional VACCG combustor.
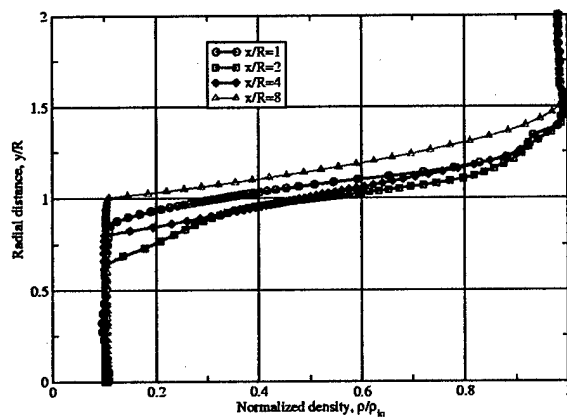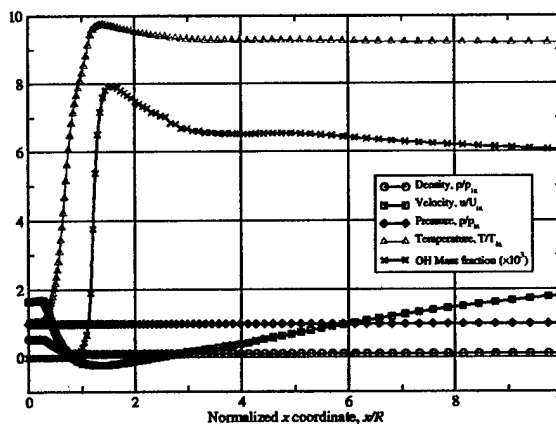
(a) Centerline
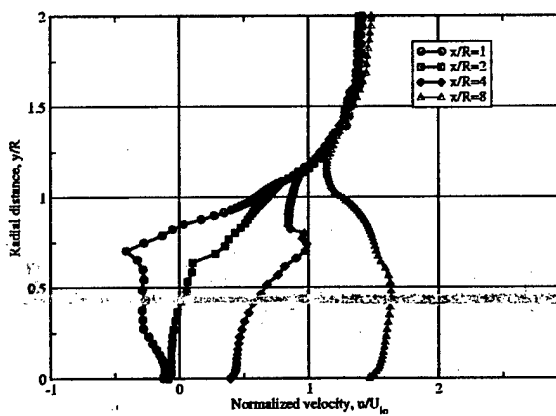
(b) Density profiles.

(c) Velocity profiles.
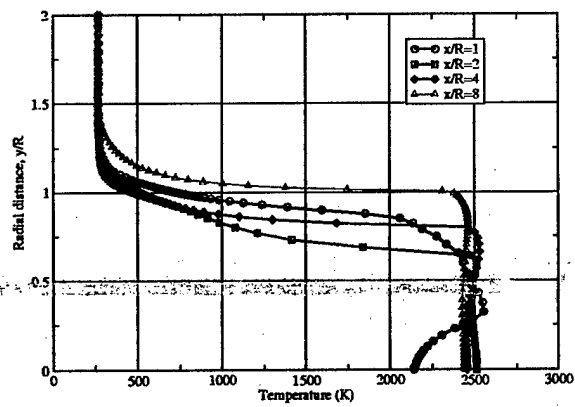
(d) Temperature profiles.

Figure 2.29: Centerline and profile data for 3-D combustor.

becomes independent of the initial condition. The temporal history beginning at $t = 27.5 ms$ is shown in Figure 2.31. The temperature distribution at $t = 45.0 ms$ is shown in Figure 2.32.

The velocity and pressure response is recorded as a function of time at $x/R = 1$ and $y/R = 1$ (*i.e.,* one radius downstream and one radius above the centerline). Subtracting the mean signal, the perturbations are shown normalized vy the inlet values in Figure 2.33(a). The mean velocity for the signal at is $15.28 \, m/s$. The responses of the mass fractions in the chemistry model are shown in Figure 2.33(b). We see four spikes in the OH mass-fraction response before $t = 0.015 \, s$ These spikes are associated with the transition from the initial condition to the unsteady solution. The presence of carbon dioxide (CO_2)indicates combustion and is necessarily 180° out-of-phase with the methane (CH_4) mass fraction.

A second recording is recorded at $x/R = 8$ to measure a correlation between the signals. The responses at $x/R = 1$ and $x/R = 8$ are shown together in Figure 2.34(a). The mean velocity at $x/R = 8$ is $27.27 \, m/s$. A fast Fourier transform (FFT) of the data after $t = 0.2$ is shown in Figure 2.34(b). The FFT reveals the dominant frequency in the signal occurs at $158.7 \, Hz$ with a sub-harmonic at $380.9 \, Hz$.

Discussion of the Starting Procedure

In the beginning of the project, starting the flame was computational challenge because no hot, ignition source exists to induce chemical reactions and subsequent combustion. For example, in external aerodynamics of re-entry vehicles, chemical reactions of air species take place aft of a shock wave. In other internal-flow cases, a pre-heated wall increases the flow temperature to a range where chemical kinetics become important. In the experimental combustor rig, a spark ignites the fuel/air mixture; however, no such numerical analog is readily apparent.

To circumvent this problem, we use the capabilities of $\mathcal{GASP}$ to our advantage. Specifically, we can map a small sub-set of species to a larger model. This is important because the flow can be initialized using very few species and then converted to the full-specie model. To that end, we initialize the flow with a cold-flow air/methane mixture on a coarse mesh. This is a very rapid process which establishes a good initial guess to the cold-flow simulation for a small number of grid points and just two species. Needless to say, the computational time required for a full-specie model on a fine mesh would be substantially larger.

With the density, velocity and pressure fields well-defined for the correct equivalence ratio and geometry, we perform two conversions. First, we convert the air density to 79% nitrogen and 21% oxygen (by mole), while copying the methane density unchanged. There are 12 species in the Bowmann/Seery model, and the remaining specie densities in the model are set to zero. Secondly, the temperature in the combustion zone is increased artificially by lowering the specie densities while holding the pressure constant. Because $T = p/(\sum \rho_i R_i)$, a decrease in all the densities, ρ_i, results in an increase in the temperature, T. We decrease the densities by a factor of ten which gives a combustion-zone temperature in the range of the adiabatic flame temperature. This solutin is then used with chemical kinetics active until the flow reaches a physically realistic solution.

The experience with numerically "igniting" internal combustor flows has demonstrated the need to place restrictions on the magnitude of the chemical source terms. Many methods for starting the chemistry were tried, but only the above procedure proved to be well behaved. Often times, the simulation quickly diverged as the mixture progressed to unrealistic states
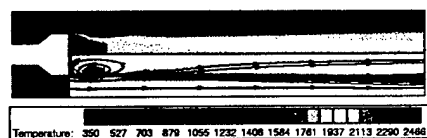
(a) t=0ms
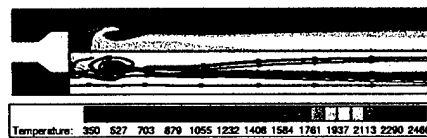
(b) t=2.5ms
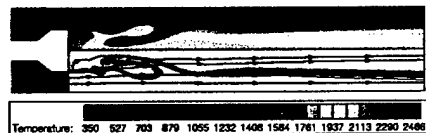
(c) t=5.0ms
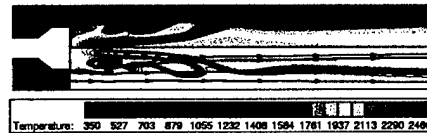
(d) t=7.5ms
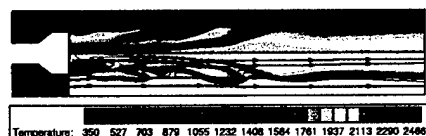
(e) t=10.0ms
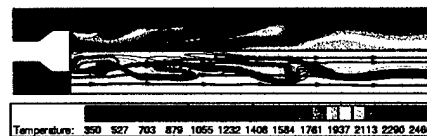
(f) t=12.5ms
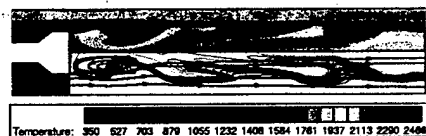
(g) t=15.0ms

(h) t=17.5ms

Figure 2.30: Temperature contours for axi-symmetric, two-dimensional blunt-body combustor without methane injection. Sequence shows temporal history beginning with a steady, initial condition.
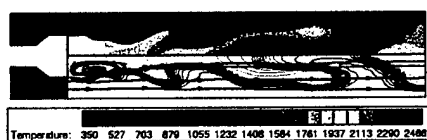
(a) t=27.5ms
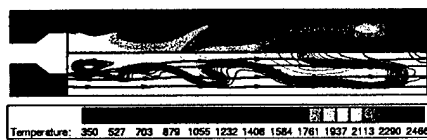
(b) t=30.0ms
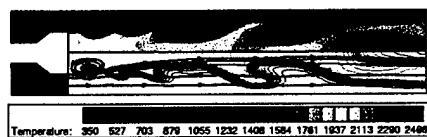
(c) t=32.5ms
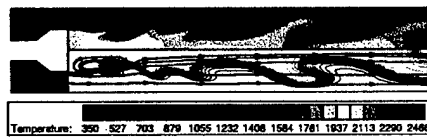
(d) t=35.0ms
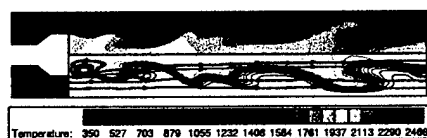
(e) t=37.5ms
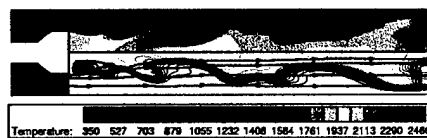
(f) t=40.0ms
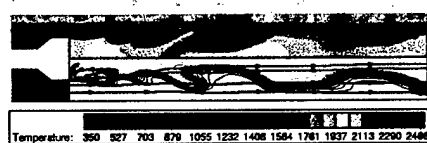
(g) t=42.5ms
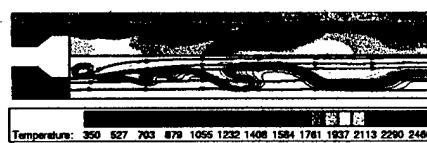
(h) t=45.0ms

Figure 2.31: Temperature contours for axi-symmetric, two-dimensional blunt-body combustor without methane injection. Sequence shows temporal independence from initial condition.
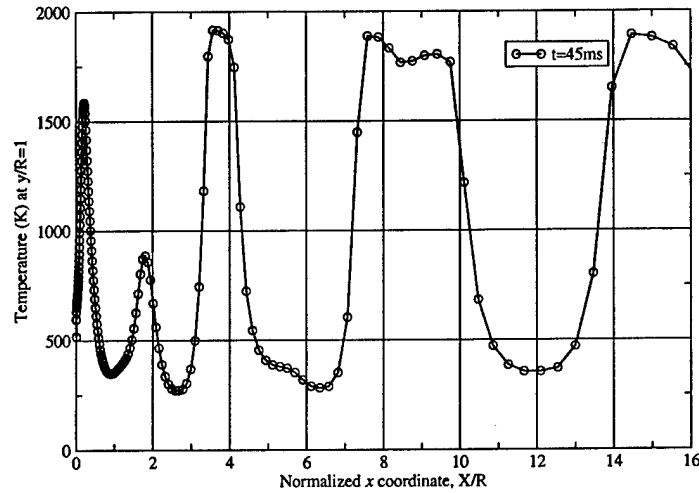
Figure 2.32: Temperature profile at $y/R = 1$.

(*e.g.,* infinite temperatures, negative densities or pressures). One procedure for igniting the flow that was very stiff involved increasing the pressure for a small number of cells in the recirculation region. This resulted in an increase in the temperature, but caused a tremendous disturbance in the velocity and pressure fields. As a result, the maximum, stable time step was a very small value on the order of $\Delta t = 10^{-9}$ *sec*. This necessity brought about the invention of a procedure that we call "Damkohler limiting". As a result of this work, an AIAA paper was produced which will be presented at the 43rd Aerospace Science Meeting on January, 2005. We include below an excerpt from that paper in this report.
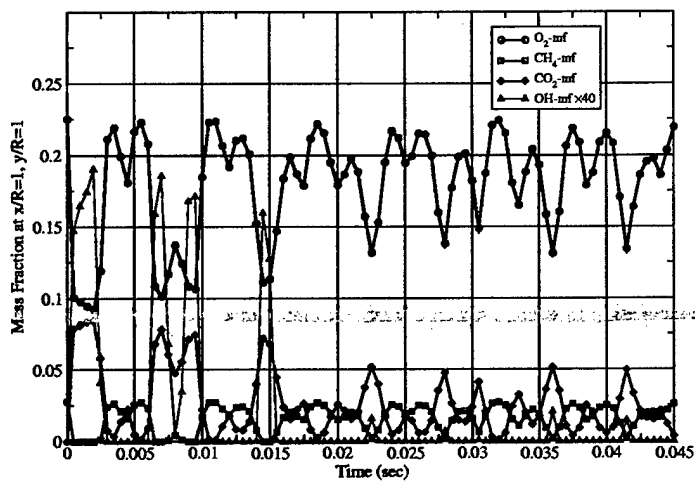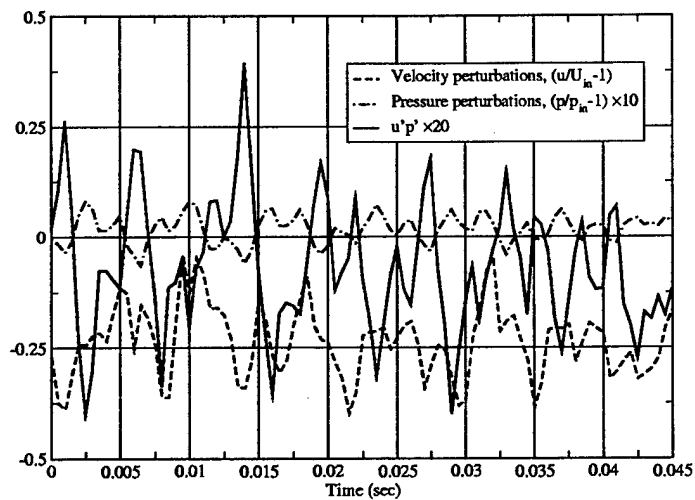
(b) Mass fraction response.

Figure 2.33: Time history of x-component of velocity and mass-fractions at $x/R = 1$ and $y/R = 1$.
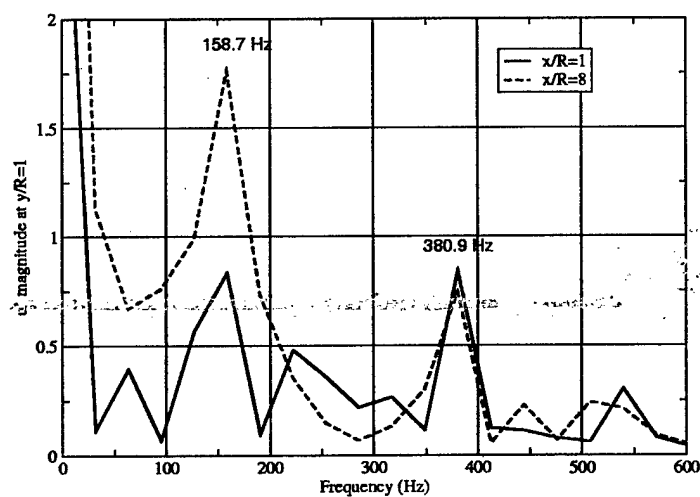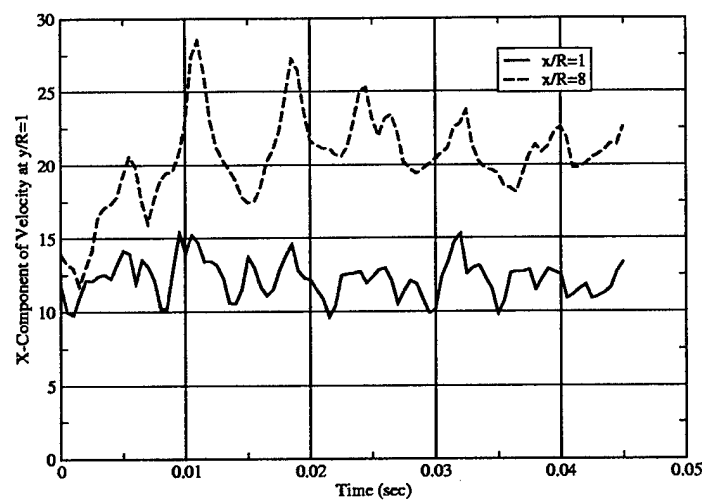
(b) FFT of signal.

Figure 2.34: Time history of x-component of velocity at $x/R = 1$ and $x/R = 8$ and $y/R = 1$.

(Excerpt from AIAA Paper 2005-1400)

The Damkohler Number

The Damkohler number is generically defined as the ratio of the fluid-dynamic time scale to a second physically relevant time scale such as chemical kinetics, binary diffusion or heat and momentum transfer. For example, we can consider the inverse of the cell Reynolds number as a Damkohler number for viscous diffusion as follows

$$Da_\mu = 1/Re_{\Delta x} = \frac{\mu}{\rho U \Delta x} = \frac{(\Delta x/U)}{(\rho \Delta x^2/\mu)}. \tag{2.1}$$

For a viscous flow, diffusion of momentum becomes important when the viscous Damkohler number (*i.e.*, the inverse of the Reynolds number) increases. More conventionally, diffusion plays a more important role as the Reynolds number decreases. A large Damkohler number means that the time scale of interest is much smaller than the fluid-dynamic time scale. In other words, a small time scale means that the physical process associated with the scale is happening quickly compared to the convection of fluid. Likewise, a large time scale means the process is progressing slowly. This has particular relevance for chemically reacting flows where the Damkohler number is defined as

$$Da_{ch} = \frac{\tau_{fd}}{\tau_{ch}}. \tag{2.2}$$

A large Damkohler number ($Da >> 1$) means that the chemical time scale is much larger than the fluid-dynamic scale and the flow is tending toward equilibrium. Likewise, a small Damkohler number means the flow is nearly frozen since the chemical changes would be lagging far behind the fluid-dynamic changes. The local fluid-dynamic time scale, τ_{fd}, is defined here as the time required for a fluid particle to advect across one cell.

Numerical Stiffness

When a physical system has drastically different characteristic times, numerical stiffness results which limits the progression to a steady state by the smallest time. As seen in the scalar, advection equation, the affect of the source term is to constrain the time step to $min(a\Delta x, 2\tau)$. In finite-rate chemical kinetics, $\tau_{ch} \to 0$ as a mixture approaches equilibrium for a fixed flow speed. Therefore, rapid chemical kinetics causes numerical stiffness because the numerical time step must approach zero in order to maintain stability. This is undesirable for steady-state problems and Godfrey [3] shows that implicit algorithms bypass this transient stiffness by re-scaling the chemical characteristic time.

Eberhardt and Imlay [4] show that the fastest reaction slows all reactions, and thus slows down steady-state convergence. Any time scale that is shorter than the fluid-dynamic scale is considered a "sub-grid" time scale. The fluid-dynamic scale is the time required for a fluid particle to advect across a cell. If the chemical composition is changing so fast that the mixture reaches equilibrium before crossing a cell, then the reaction rates can be reduced to delay the rate at which equilibrium is reached. In other words, there is no need to resolve chemical time scales which are smaller than the grid can resolve. Eberhardt and Imlay use a maximum Damkohler number of ten ($Da_{max} = 10$) and remark that the effect is to smear shocks slightly. We will see in our results that the maximum error introduced by the limiting occurs at a shock discontinuity.

Chemical Time Scales

For unsteady flow computations, the Damkohler number for chemistry is defined as the ratio of fluid-dynamic to chemical time scales. For the remainder of this paper, the chemical Damkohler number will be denoted as

$$Da \equiv \frac{\min\{\tau_{fd}, \Delta t\}}{\tau_{ch}}. \tag{2.3}$$

Generally, the chemical time scale is inversely proportional to the fastest reaction rate in the model. Damkohler limiting modifies the fastest reaction rate while maintaining the equilibrium constant (*i.e.*, the backward rate is changed to compensate for the change in the forward rate so that their ratio remains the same).

We can represent a general chemical-kinetic system composed of N species and J reactions as follows

$$\nu'_{1,j}X_1 + \nu'_{2,j}X_2 + \cdots + \nu'_{N,j}X_N \rightleftharpoons \nu''_{1,j}X_1 + \nu''_{2,j}X_2 + \cdots + \nu''_{N,j}X_N$$
$$j = 1, 2, ..., J, \tag{2.4}$$
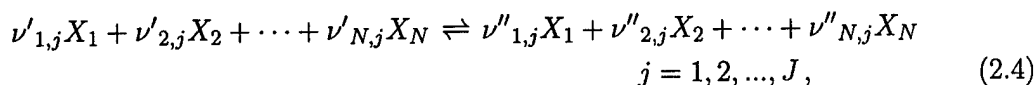
where $\nu'_{i,j}$ and $\nu''_{i,j}$ are the stoichiometric coefficients of species X_i in the *jth* reaction. The rate of production of species s is given as

$$\frac{d\rho_i}{dt} = \mathcal{M}_i \sum_{j=1}^{J}(\nu''_{i,j} - \nu'_{i,j})\left[k_{f,j}\prod_{l=1}^{N}(\frac{\rho_l}{\mathcal{M}_l})^{\nu'_{l,j}} - k_{b,j}\prod_{l=1}^{N}(\frac{\rho_l}{\mathcal{M}_l})^{\nu''_{l,j}}\right], \qquad i = 1, 2, ..., N, \tag{2.5}$$

where $k_{f,j}$ and $k_{b,j}$ are the forward and backward reaction rates. The forward rates are determined from the Arrhenius equation

$$k_f = C\,T^{\eta}\,e^{-\epsilon/kT}, \tag{2.6}$$

and the backward rates are determined from the ratio of the forward rate to the equilibrium constant

$$k_b = \frac{k_f}{K_e}. \tag{2.7}$$

The equilibrium constants are determined from either the Arrhenius equation, equilibrium curve fits, or from the McBride Curve fits and the minimization of Gibbs free energy.

Bimolecular Reaction   We are interested in the chemical time scale for the elementary reactions that compose a chemical kinetics model. Following Turns [5], we consider the following bimolecular reaction

$$A + B \rightarrow \text{products} \tag{2.8}$$

and its rate equation

$$\frac{d[A]}{dt} = -k\,[A][B]. \tag{2.9}$$

We substitute the defect variable, $x \equiv [A] - [A]_0 = [B] - [B]_0$, into the rate equation and integrate to yield

$$\int \frac{dx}{(x + [A]_0)(x + [B]_0)} = -kt + C. \tag{2.10}$$

Reaction	Example	τ_{ch}
$2\,A \rightarrow$ products	$2\,O \rightarrow O_2$	$\dfrac{e-1}{2[A]_0\,k}$
$A + M \rightarrow$ products $+ M$	$H_2O + M \rightarrow H + OH + M$	$\dfrac{1}{[M]_0\,k}$
$2\,A \rightarrow$ products $+ A$	$2\,O_2 \rightarrow 2\,O + O_2$	$\dfrac{e-1}{[A]_0\,k}$
$A + B \rightarrow$ products	$H_2 + O_2 \rightarrow 2\,HO$	$\dfrac{\mathcal{L}(x)}{([A]_0 - [B]_0)\,k}$
$A + B + M \rightarrow$ products $+ M$	$N + O + M \rightarrow NO + M$	$\dfrac{\mathcal{L}(x)}{([A]_0 - [B]_0)\,k[M]}$

Table 2.2: Chemical time constants where $x \equiv [A]_0/[B]_0$ and $[A]$ is assigned to the smaller concentration.

The left-hand integral can be determined to be

$$\int \frac{dx}{(x + [A]_0)(x + [B]_0)} = \frac{1}{[A]_0 - [B]_0} \ln\left(\frac{[B]}{[A]}\right). \tag{2.11}$$

and setting this result equal to the right-hand side of Eqn. (2.10), we can solve for the temporal decay of $[A]/[B]$ as follows

$$\frac{[A]}{[B]} = \frac{[A]_0}{[B]_0} \exp\{([A]_0 - [B]_0)\,kt\}. \tag{2.12}$$

This expression is used to determine the time constant for the decay of the specie concentrations.

Definition: Time Constant The *time constant* is defined as the time elapsed for an initial concentration to decay by $1/e$. Assigning $[A]_0$ to be the smaller of the two concentrations, we solve Eqn. (2.12) for τ_{ch} by solving for the time when $[A]/[A]_0 = 1/e$ where we use the fact that $[B]/[B]_0 = ([A]_0/[B]_0)([A]/[A]_0 - 1) + 1$. We obtain the time constant for a bimolecular reaction as

$$\tau_{ch} = \frac{\mathcal{L}\{[A]_0/[B]_0\}}{([A]_0 - [B]_0)\,k} \tag{2.13}$$

where

$$\mathcal{L}\{[A]_0/[B]_0\} \equiv \ln \frac{[A]/[A]_0}{[B]/[B]_0}\bigg|_{[A]/[A]_0=1/e} = -\ln\left[e - (e-1)\left(\frac{[A]_0}{[B]_0}\right)\right]. \tag{2.14}$$

Table 2.2 lists the chemical time scales for several common elementary reactions.

A General Method for Computing the Chemical Time Constant   As demonstrated above, the analytical expression for the chemical time constant depends on the form of the elementary reaction. Rather than devise expressions for every possible reaction, we seek a general method which applies to every case. In the context of Eqn. (2.4), consider the jth chemical reaction in a general chemical-kinetics model

$$\nu'_{1,j}X_1 + \nu'_{2,j}X_2 + \cdots + \nu'_{N,j}X_N \rightleftharpoons \nu''_{1,j}X_1 + \nu''_{2,j}X_2 + \cdots + \nu''_{N,j}X_N. \tag{2.15}$$
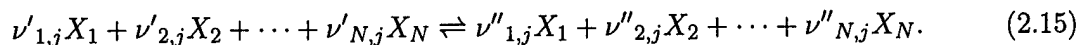
The defect law for each specie can be written as follows

$$\frac{[X_1] - [X_1]_0}{\nu''_{1,j} - \nu'_{1,j}} = \frac{[X_2] - [X_2]_0}{\nu''_{2,j} - \nu'_{2,j}} = \cdots = \frac{[X_N] - [X_N]_0}{\nu''_{N,j} - \nu'_{N,j}}. \tag{2.16}$$

We can compute the chemical time scale numerically by solving an ordinary differential equation for the specie with the smallest negative defect. That is, we assume that $\nu_{1,j} \equiv \nu''_{1,j} - \nu'_{1,j} < 0$ and that the species are listed in order of increasing defect

$$\frac{[X_1]_0}{|\nu_{1,j}|} < \frac{[X_2]_0}{|\nu_{2,j}|} < \cdots < \frac{[X_N]_0}{|\nu_{N,j}|}. \tag{2.17}$$

Under these conditions, we can solve the following ODE for the decay of $[X_1]$

$$\frac{d[X_1]}{dt} = \nu_{1,j}\, k_{f,j} [X_1]^{\nu'_{1,j}} [X_2]^{\nu'_{2,j}} \cdots [X_N]^{\nu'_{N,j}}. \tag{2.18}$$

The defect law (Eqn. (2.16)) can be used to write all the specie concentrations if Eqn. (2.18) in terms of $[X_1]$. A similar ODE can be written for the smallest decreasing specie in the backward reaction with rate coefficient $k_{b,j}$.

To solve Eqn. (2.18) for the chemical time scale we use a second order mid-point method to determine the time when the specie decays by a ratio of $1/e$. We first make a first-order approximation using the Euler-explicit method for an initial guess

$$[X_1]^* = [X_1]_0 + \left[\frac{d[X_1]}{dt}\right]_0 \tau_{ch}^*. \tag{2.19}$$

Solving for τ_{ch}^* and noting that $[X_1]^*/[X_1]_0 = 1/e$, we have

$$\tau_{ch}^* = \left([X_1]_0 \Big/ \left[\frac{d[X_1]}{dt}\Big|_0\right]\right)(1/e - 1). \tag{2.20}$$

The second-order approximation can be written by re-evaluating the right hand side of Eqn. (2.18) using the mid-point concentration (*i.e.*, $[X_1]_0 + [X_1]'_0\,(1/2\,\tau_{ch}^*)$). Our chemical time scale for any elementary reaction can then be written as

$$\tau_{ch} = \left([X_1]_0 \Big/ \left[\frac{d[X_1]}{dt}\Big|_{1/2\tau_{ch}^*}\right]\right)(1/e - 1). \tag{2.21}$$

Fluid Dynamic Time Scales

The fluid-dynamic time scale is determined locally for each cell in the flow field. For a structured mesh in a finite-volume setting, we compute a time scale for each coordinate direction and choose the smallest one in magnitude. For our calculations, we compute the following three time scales

$$\tau_{fd_i} = \frac{2\Delta\mathcal{V}_{ijk}}{|\bar{u}_{i-1/2}|\Delta A_{i-1/2} + |\bar{u}_{i+1/2}|\Delta A_{i+1/2}}$$

$$\tau_{fd_j} = \frac{2\Delta\mathcal{V}_{ijk}}{|\bar{u}_{j-1/2}|\Delta A_{j-1/2} + |\bar{u}_{j+1/2}|\Delta A_{j+1/2}}$$

$$\tau_{fd_k} = \frac{2\Delta\mathcal{V}_{ijk}}{|\bar{u}_{k-1/2}|\Delta A_{k-1/2} + |\bar{u}_{k+1/2}|\Delta A_{k+1/2}}$$

where $\bar{u} \equiv \vec{V} \cdot \hat{n}$ is the velocity component normal to each cell face. The fluid-dynamic time scale is the minimum of the three possibilities.

Application

For each reaction (j) in a model, we determine Damkohler numbers based on the forward and backward time constants. If the larger Damkohler number exceeds a threshold (*i.e., $Da_{\max}$*), then the corresponding reaction rate is modified in such a way as to maintain the equilibrium constant. That is,

- If $Da_{f,j} > Da_{b,j}$ and $Da_{f,j} > Da_{\max}$, then the modified rate coefficient becomes

$$\tilde{k}_{f,j} = \omega\left(\frac{Da_{\max}}{\min\{\tau_{fd}, \Delta t\}}\right) \tag{2.22}$$

- If $Da_{b,j} > Da_{f,j}$ and $Da_{b,j} > Da_{\max}$, then

$$\tilde{k}_{b,j} = \omega\left(\frac{Da_{\max}}{\min\{\tau_{fd}, \Delta t\}}\right) \tag{2.23}$$

If limiting is applied to either rate coefficient, the opposite rate coefficient is adjusted maintain the following equality

$$K_{e,j} = \frac{\tilde{k}_{f,j}}{\tilde{k}_{b,j}}. \tag{2.24}$$

Because the method maintains the original law of mass action, the equilibrium distribution remains unchanged and only the *rate* to reach equilibrium altered.

In the above, $\omega = \tau_{ch}k$, which makes ω dependent on the type of reaction. However, we can assume that bimolecular reactions will occur faster than termolecular ones. If we assume that one concentration in the bimolecular reaction is much larger than the other, then ω becomes in the limit

$$\omega = \frac{1}{\max\{[A]_0, [B]_0\}}. \tag{2.25}$$

Supersonic Air Nozzle

We consider steady, supersonic flow of a five-species, expanding air mixture through a nozzle with the following inlet conditions:

$$\rho_{N_2} = 0.00048557\,kg/m^3$$
$$\rho_{O_2} = 1.55682 \times 10^{-7}\,kg/m^3$$
$$\rho_{NO} = 9.9556 \times 10^{-6}\,kg/m^3$$
$$\rho_N = 0.0146888\,kg/m^3$$
$$\rho_O = 0.00460352\,kg/m^3$$
$$U = 4000\,m/s$$
$$T = 9000\,K.$$

At this high temperature, the inlet gas is composed of primarily dissociated nitrogen ($\rho_N/\rho = 74.2\%$) and oxygen ($\rho_O/\rho = 23.2\%$) with a small amount of diatomic nitrogen (2.4%) and trace amounts of O_2 and NO.

We simulate the nozzle flow using chemical-kinetics model of Kang et al. [6] on a 11×41 mesh with uniform spacing. Time integration consists of a first-order implicit marching scheme until the relative residual tolerance declines five orders of magnitude. The distribution of Damkohler limiting is shown in Figure 2.35(a). The contours show that the Damkohler number is largest at the in-flow plane ($Da = 761.5$) where the temperature (and reaction rates) are largest and the flow speed is the smallest. As the flow expands, the temperature decreases (see Figure 2.35(b)) and the flow speed increases. Therefore, the Damkohler number decreases downstream until $Da = 42.7$ at the exit.

In order to examine the effect of Damkohler limiting on solution quality, a number of Damkohler-limited cases are run with Da_{max} ranging from $Da_{max} : 0.1 \rightarrow 10$. In Figure 2.36, we present the mass-fraction distributions for the various Damkohler numbers compared to the unlimited case. For all Damkohler numbers except $Da_{max} = 0.1$, the results are virtually identical between the unlimited and limited cases. In the most severely limited case, the primary source of the error occurs at the inlet. The trend in the mass fraction downstream of the inlet closely matches the unlimited case. We emphasize that the most severe case limits the reaction rates by a factor of 7615 smaller than the original model. However, the solution remains virtually unchanged. While the errors in Figure 2.36(b) appear to be large, the scale of the axis is very small and the peak error is less that 0.05% at $Da_{max} = 1.0$.

(End of Excerpt from AIAA Paper 2005-1400)

2.3 Implementation of Sensitivity-Equation Method in GASP

Inviscid Sensitivity Modifications

One objective of the Phase II portion of this project is to incorporate the sensitivity software that has been developed in the stand-alone sensitivity solver, $\mathcal{SENSE}$, into AeroSoft's commercial flow solver, $\mathcal{GASP}$. The reason for this transition is that time-accurate calculations require a tight coupling between the flow and sensitivity solvers. The stand-alone capability (which is so beneficial for steady-state calculations) is still available through $\mathcal{GASP}$, but
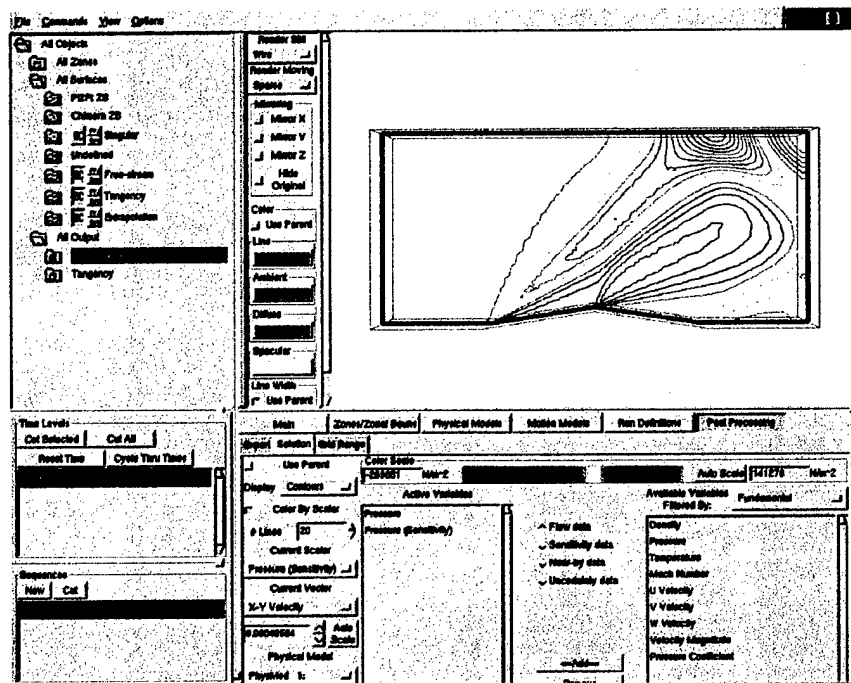
Figure 2.37: GASP graphical user interface displaying the diamond-airfoil sensitivity solution.

many features that have been developed for the flow solver can also be applied to sensitivity problems. These include the user interface, distributed parallel, overset methods, implicit and explicit temporally accurate methods, and many thermodynamic and chemical reaction models.

As a way of beginning the testing under the $\mathcal{GASP}$ framework, an inviscid flow and sensitivity calculation were conducted for supersonic flow over a diamond airfoil. The user interface for this problem is shown in Figure 2.37 where the design variable is the free-stream velocity. From the interface, the user can output data of four different types: flow data, sensitivity data, near-by data, or uncertainty data. Very few modifications are required by the user to transform the GUI from running a flow problem to running a sensitivity problem.

The pressure distribution along the airfoil for a 5% perturbation from $M_\infty = 2.0$ to $M_\infty = 2.1$ is shown in Figure 2.38. The near-by approximation compares well with a new calculation at $M_\infty = 2.1$.

Viscous and Turbulent Sensitivity Modifications

A subsonic, flat-plate boundary layer flow is used to verify that the sensitivity equation method is being utilized correctly for the eddy-viscosity models of $\mathcal{GASP}$. Each of these models has been tested and incorporated into AeroSoft's stand-alone sensitivity solver, $\mathcal{SENSE}$. However, because the discretization methods in $\mathcal{GASP}$ are slightly different, the coding task was not as straight-forward as importing the pre-existing code. After completing coding for viscous fluxes and turbulence source terms, the sensitivity results for three turbulence

Diamond Airfoil Sensitivity to Free-stream Velocity

Near-by Flow Approximation at M=2.1
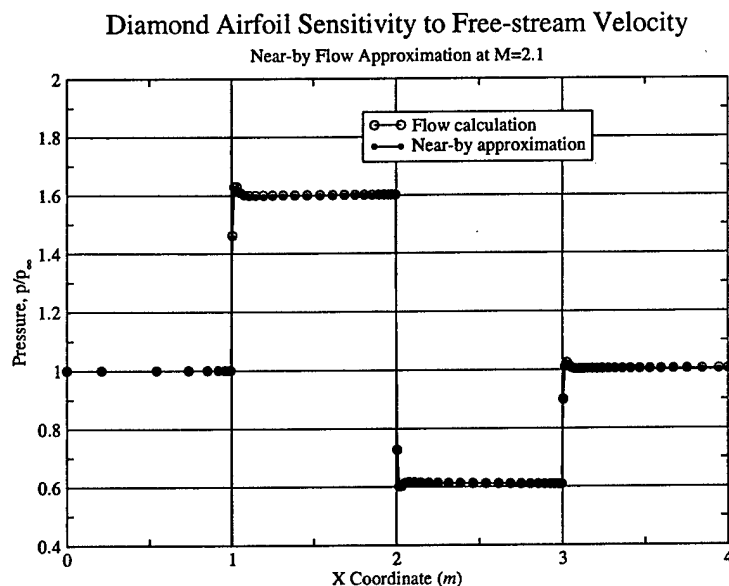
Thu Oct 31 11:38:01 2002

Figure 2.38: Near-by pressure approximation compared to a new calculation to for the diamond airfoil sensitivity to free-stream velocity..

models are shown in Figure 2.39. These results are consistent with what has been obtained using $\mathcal{SENSE}$ in Godfrey and Cliff [7].

Time-Accurate Numerics

The final modification needed to implement the sensitivity software in $\mathcal{GASP}$ involved the time-marching schemes. Sensitivity modifications have been made in $\mathcal{GASP}$ in order to use the explicit and implicit time-accurate algorithms. This process required changing data structures from manipulating only flow-related data to manipulating general sets of data (flow and sensitivity). As such, a level of abstraction had to be added to the solution-related data structures. Being written in C++, $\mathcal{GASP}$ is easily adapted to such an abstraction. With the time-accurate capability complete, a user can run time-accurate sensitivity calculations in conjunction with either fixed or time-accurate flow solutions.

As a verification case, the variable accuracy Runge-Kutta and quasi-Newton algorithms have been applied to a typical shock-tube case where the design variable is the high-pressure-region's pressure (see also Appel [8]). The sensitivity results for various time-integration schemes are shown in Figure 2.40 with comparison to shock-tube theory. This problem was run by ICAM during the Phase I project and is now being reproduced for the first time with the newly developed $\mathcal{GASP}$ capability. Since the results are in very good agreement with the theoretical sensitivities (except at the discontinuities), we are confident that the schemes have been implemented correctly for time-accurate sensitivity calculations. Thus, we could move forward toward investigating the combustion-related sensitivity problems.

Turbulent Flat Plate Sensitivity to Edge Velocity
$Re_L = 2 \times 10^6$, $M_\infty = 0.3$
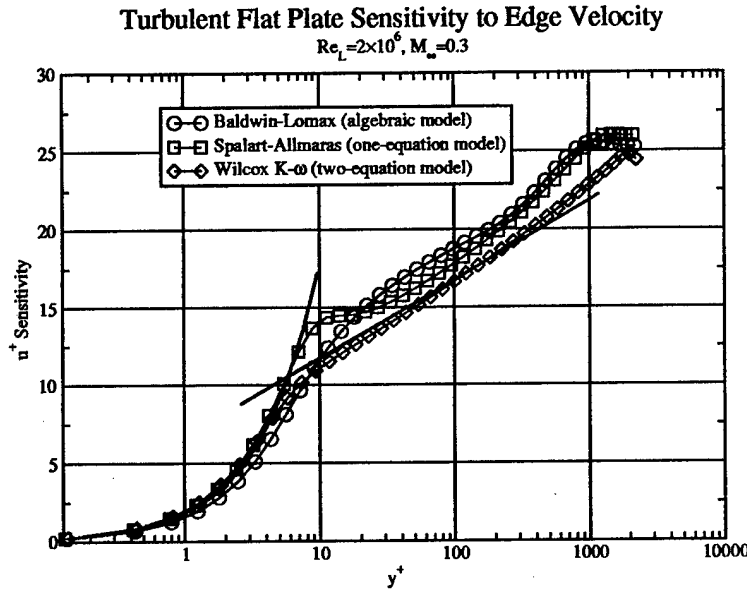
Figure 2.39: Sensitivity results for a turbulent flat plate.

2.4 Feedback Control of 1-D Model Problem

This section of the report is similar in style to a technical paper rather than a step-by-step summary of the activities carried out. We describe here the work completed in controlling a model, acoustic-instability problem.

One-dimensional Non-linear Flow Equations

In Venkateswaran *et al.* [9] and Wang *et al.* [10], the authors use a boundary condition which couples the pressure and velocity perturbations to cause an initial acoustic wave to become unstable. A one-dimensional, pressure perturbation grows, at first linearly, until reaching a non-linear limit cycle. We wish to reproduce these results and then consider some control methods to suppress the instability.

For generality, consider the one-dimensional, unsteady flow of a compressible, perfect gas in a tube of constant area. Conservation of mass, momentum and energy lead to the following partial differential equation (PDE)

$$\frac{\partial \mathbf{Q}(t,x)}{\partial t} + \frac{\partial \mathbf{F}\left(\mathbf{Q}(t,x)\right)}{\partial x} = \mathbf{S}(t,x), \quad 0 < x < L, \quad t > 0, \tag{2.26}$$

where

$$\mathbf{Q} = \begin{bmatrix} \rho \\ \rho u \\ \rho e_0 \end{bmatrix}, \quad \mathbf{F} = \begin{bmatrix} \rho u \\ \rho u^2 + p \\ \rho u h_0 \end{bmatrix}, \quad \text{and} \quad \mathbf{S} = \begin{bmatrix} 0 \\ 0 \\ S_e(t,x) \end{bmatrix}.$$

In these equations

- $\rho(t,x)$ is the density,

- $u(t,x)$ is the velocity,
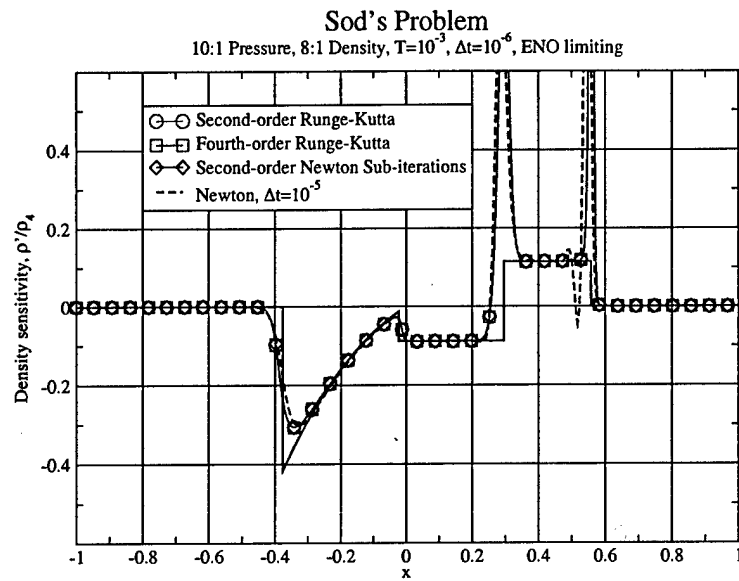
(a) Density sensitivity.
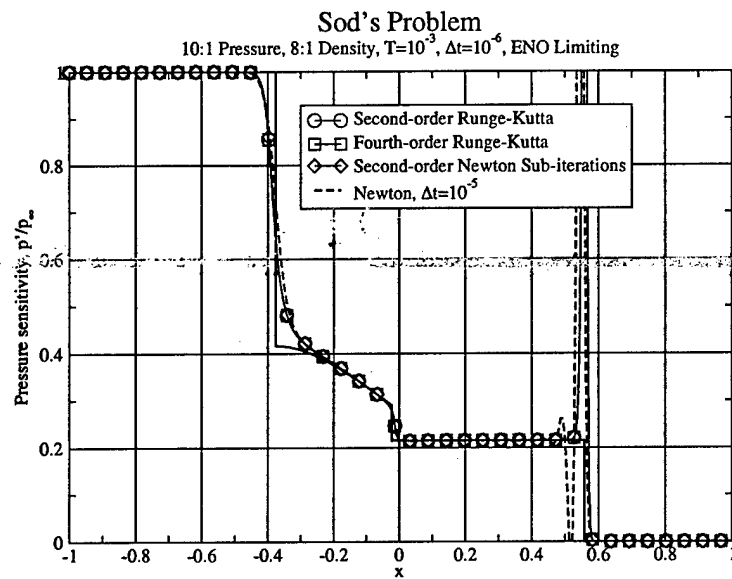
(b) Pressure sensitivity.

Figure 2.40: Sensitivity solution to the 10:1 shock tube.
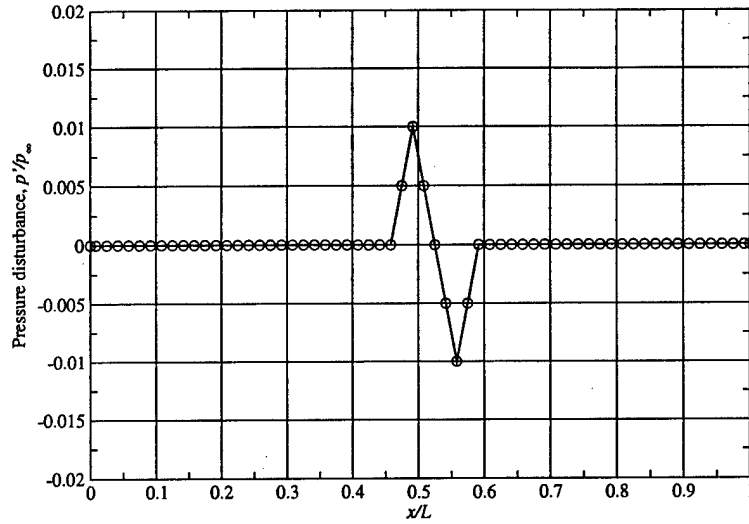
Figure 2.41: Initial triangular pressure pulse for one-dimensional control.

- $e(t, x)$ is the internal energy per unit mass,

- $e_0(t, x)$ is the total energy per unit mass $(= e + \frac{u^2}{2})$,

- $p(t, x)$ is the pressure $(p = (\gamma - 1)\rho e)$,

- $h_0(t, x)$ is the stagnation enthalpy per unit mass $(= e_0 + \frac{p}{\rho})$, and

- $S_e(t, x)$ represents input of thermal energy (*e.g.* watts/m^3).

Here γ is the usual ratio of specific heats.

We are interested in the growth/control of a triangular, pressure pulse shown in Figure 2.41. The initial flow state consists of a uniform, subsonic flow with a $\pm 1\%$ perturbation in the pressure at the mid-section of the pipe. The length and conditions of the pipe are consistent with those experienced in the VACCG combustor.

$$
\begin{aligned}
L &= 1.4732\,m \\
\rho_0 &= 1.2042\,kg/m^3 \\
u_0 &= 15\,m/s \\
p_0 &= 93760\,N/m^2 \\
\gamma_0 &= 1.396
\end{aligned}
$$

The inflow boundary condition described earlier couples pressure and velocity perturbations to sustain an aero-acoustic instability. The boundary condition can be conceptualized as a collapsed-combustion zone where pressure perturbations lead to in-phase velocity perturbations. This boundary condition is a simplification of the role played by combustion in the instability mechanism. The coupled boundary condition [10] satisfies the following relationship:

$$
u_1' = \left[1 + \alpha \left(\frac{p_1'}{p_0} \right) \right] \frac{\rho_0 u_0}{\rho_1} - u_0 \tag{2.27}
$$

where we have selected $\alpha = 1$ for all the calculations. The state at the boundary face is given the subscript "1". The "0" subscript denotes a reference state which is the constant flow about which we make the linearization. Perturbations are denoted with a single prime, $(e.g., u' \equiv u - u_0)$. To complete the boundary condition, pressure disturbances are extrapolated from the interior and the entropy (p/ρ^γ) is held constant. The outflow boundary serves as a node for the pressure wave. All variables are extrapolated except the pressure, which is held constant.

Linear System

Assuming smooth solutions, the quasi-linear form of Eqn. (2.26) is written

$$\frac{\partial \mathbf{Q}(t,x)}{\partial t} + \frac{\partial \mathbf{F}}{\partial \mathbf{Q}}\frac{\partial \mathbf{Q}}{\partial x} = \mathbf{S}(t,x),$$

where

$$\frac{\partial \mathbf{F}}{\partial \mathbf{Q}} = \begin{bmatrix} 0 & 1 & 0 \\ -(3-\gamma)\frac{u^2}{2} & (3-\gamma)u & \gamma-1 \\ (\gamma-1)u^3 - \gamma u e_0 & \gamma e_0 - 3\frac{\gamma-1}{2}u^2 & \gamma u \end{bmatrix}. \tag{2.28}$$

We assume an underlying uniform, steady flow and write

$$\mathbf{Q}(t,x) = \mathbf{Q}_0 + \tilde{\mathbf{Q}}(t,x),$$

where $\mathbf{Q}_0$ is the constant vector value of the conserved quantities in the unperturbed flow, and $\tilde{\mathbf{Q}}(t,x)$ is a perturbation. The temporal history of $\tilde{\mathbf{Q}}(t,x)$ is described by the linear PDE

$$\frac{\partial \tilde{\mathbf{Q}}(t,x)}{\partial t} + \left.\frac{\partial \mathbf{F}}{\partial \mathbf{Q}}\right|_0 \frac{\partial \tilde{\mathbf{Q}}}{\partial x} = \mathbf{S}(t,x). \tag{2.29}$$

Primitive Variable Formulation

For several purposes, such as the discussion of boundary conditions, it is of interest to consider a change of dependent variables from the conservative set (Q) to so-called primitive variables. Here we choose

$$\mathbf{q} = \begin{bmatrix} \rho \\ u \\ p \end{bmatrix},$$

where, as noted above, ρ is the density, u is the velocity, and p is the pressure. It can be readily verified that the conservative and primitive variables are related according to:

$$\mathbf{q}(\mathbf{Q}) = \begin{bmatrix} \mathbf{Q}_1 \\ \mathbf{Q}_2/\mathbf{Q}_1 \\ (\gamma-1)\left[\mathbf{Q}_3 - \mathbf{Q}_2^2/(2\mathbf{Q}_1)\right] \end{bmatrix} \quad \text{and} \quad \mathbf{Q}(\mathbf{q}) = \begin{bmatrix} \mathbf{q}_1 \\ \mathbf{q}_1\mathbf{q}_2 \\ \frac{\mathbf{q}_3}{(\gamma-1)} + \frac{1}{2}\mathbf{q}_1\mathbf{q}_2^2 \end{bmatrix}.$$

The Jacobians of these transformations are given by

$$\frac{\partial \mathbf{Q}}{\partial \mathbf{q}} = \begin{bmatrix} 1 & 0 & 0 \\ u & \rho & 0 \\ u^2/2 & \rho u & 1/\gamma-1 \end{bmatrix}, \tag{2.30}$$

and by

$$\frac{\partial \mathbf{q}}{\partial \mathbf{Q}} = \begin{bmatrix} 1 & 0 & 0 \\ -u/\rho & 1/\rho & 0 \\ (\gamma-1)u^2/2 & -(\gamma-1)u & \gamma-1 \end{bmatrix}. \tag{2.31}$$

The linearized PDE for the primitive variables is

$$\frac{\partial \tilde{\mathbf{q}}(t,x)}{\partial t} + \mathbf{A}\frac{\partial \tilde{\mathbf{q}}}{\partial x} = \hat{\mathbf{S}}(t,x), \tag{2.32}$$

where

$$\mathbf{A} = \begin{bmatrix} u & \rho & 0 \\ 0 & u & 1/\rho \\ 0 & \gamma p & u \end{bmatrix}, \quad \hat{\mathbf{S}} = \begin{bmatrix} 0 \\ 0 \\ (\gamma-1)S_e(t,x) \end{bmatrix}. \tag{2.33}$$

Notice that the linearized system in primitive variables take the form of a state-space system

$$\dot{\mathbf{w}} = [\mathbf{A}]\mathbf{w} + [\mathbf{B}]\mathbf{u} \tag{2.34}$$

where $\mathbf{w}$ represents perturbations in the primitive flow variables and $\mathbf{u}$ is a vector containing zeros and the control variable, which we will discuss later.

Uncontrolled Response

In the uncontrolled case (*i.e.*, $S_e = 0$), the temporal response of the pressure at the inflow boundary is shown in Figure 2.42(a) for the both the non-linear (Eqn. (2.26)) and linear (Eqn. (2.32)) systems. The envelope of the response is given in Figure 2.42(b) which shows the peak values of each oscillation. For the remainder of the report, we use the envelopes of the response for clarity and to reduce the amount of ink in the figures.

The linear and non-linear formulations agree well with one another until the limit cycle begins. The linear system predicts continued growth whereas the non-linear terms cause a limit cycle at $t \approx 1.6\,sec$. The magnitude of the limit cycle is approximately $p/p_0 = 6.3\%$ with a frequency of 54.93 Hz (approximately $4L/a_0$).

Control Method

We postulate a control in our problem which represents the input of thermal energy on the interior of our spatial interval $[0, L]$. The mathematical model is represented as

$$S_e(t,x) = v_h(t)b_h(x), \tag{2.35}$$

where b_h is a fixed spatial function, while the control amplitude is modulated by the time function v_h. Our main purpose is to study the possibility of stabilizing the system through appropriate feedback control.

The b_h term represents heat addition and is loosely associated with injected methane fuel in the combustor problem. The heat addition is distributed in space according to a standard normal distribution (*i.e.*, the Gaussian distribution) which can be written as

$$\mathcal{G}(\xi; \mu, \sigma) \equiv \frac{1}{\sqrt{2\pi}}\exp\{-\frac{\xi^2}{2}\}, \quad \text{where} \quad \xi \equiv \frac{x-\mu}{\sigma}. \tag{2.36}$$
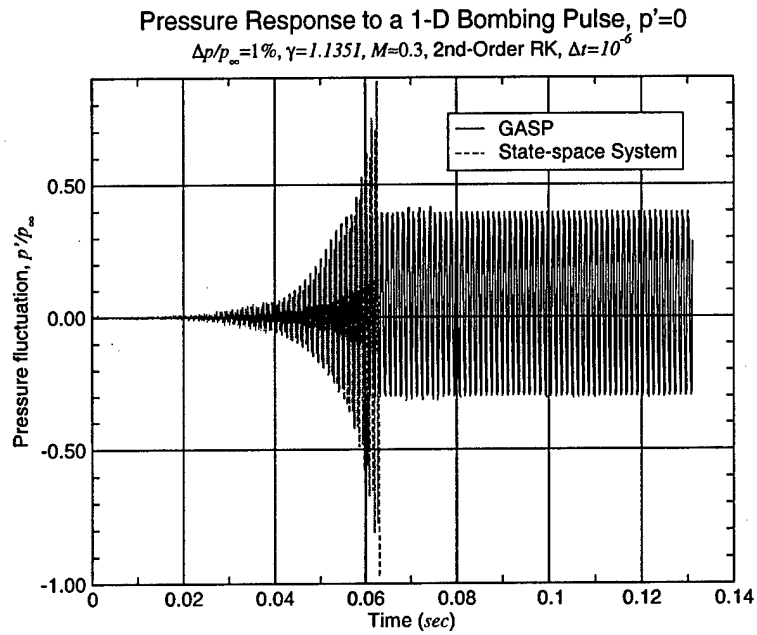
(a) Linear and non-linear response.
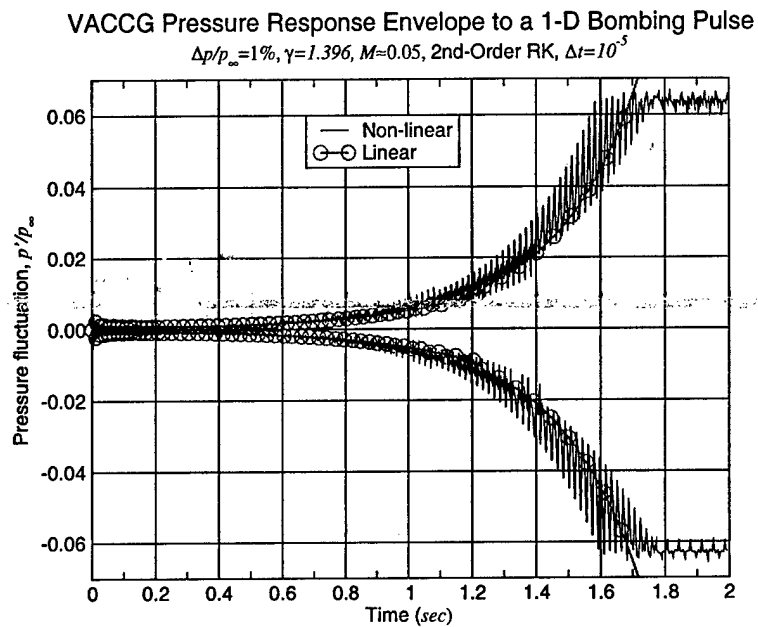
(b) Envelopes of response.

Figure 2.42: Pressure response and envelope for both the linear and non-linear systems.
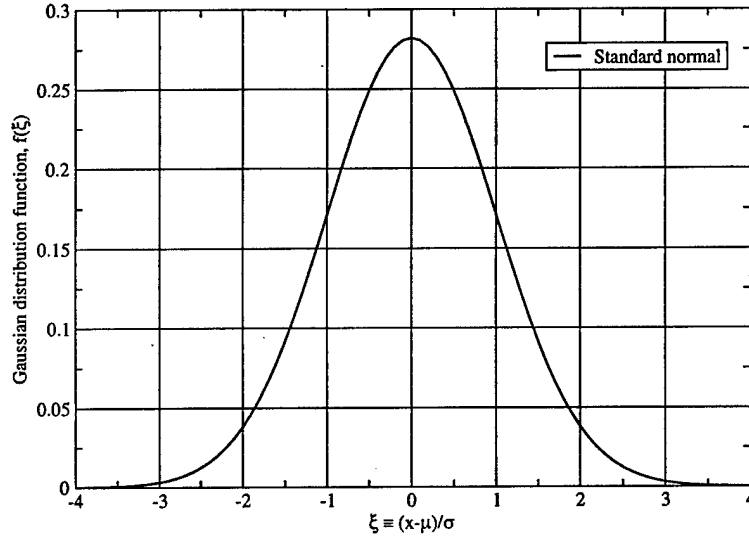
Figure 2.43: Gaussian distribution used in model for combustion control.

This distribution is shown in normalized form in Figure 2.43. The mean of the distribution is represented by μ and the variance by σ; the integral under the Gaussian distribution is unity. Our control is chosen such that the total amount of heat added to the system is a fraction of the amount necessary to produce thermal choking. That is,

$$b_h(\xi) = \epsilon \, \Delta h_0^* \mathcal{G}(\xi; \mu, \sigma). \qquad (2.37)$$

In Eqn. (2.37), $\Delta h_0^* \equiv h_0^* - h_0$ is the amount of heat-addition required to produce thermally choked flow. From Anderson [11], the amount of heat addition needed for choking can be determined from

$$\frac{h_0}{h_0^*} = \frac{2\,(\gamma+1)M^2}{(1-\gamma M^2)^2}\left[1 + \frac{\gamma-1}{2}M^2\right]. \qquad (2.38)$$

We choose $\epsilon = 10^{-3}$ (*i.e.*, 0.1% of choked heat addition) and the control is applied at the front of the domain by selecting $\mu = L/10$ and $\sigma = L/60$.

Abstract LQR control problem

Our objective is to stabilize the non-linear system described by the Euler equations subject to the coupled boundary conditions. One way to construct a stabilizing controller is to formulate an optimal-control problem with linearized dynamics and a quadratic cost functional. The dynamics are linearized about a uniform steady flow and our cost functional is defined using inner products as

$$J(\mathbf{u}) = \int_0^\infty \frac{1}{2}\left\{\left(\int_0^L \mathbf{w}^T\mathbf{Q}\mathbf{w}\,dx\right) + \mathbf{u}^T\mathbf{R}\mathbf{u}\right\}\,dt, \qquad (2.39)$$

where we select $\mathbf{Q} = \mathrm{diag}\{Q_\rho, Q_u, Q_p\}$ to be a diagonal matrix of prescribed non-negative functions that penalize perturbations in density, velocity, and pressure, respectively. $\mathbf{R}$ is

a matrix of prescribed positive scalar weights on the control, $\mathbf{u}$. In our case, $\mathbf{R}$ and $\mathbf{u}$ are scalar values.

We use a finite-volume formulation to construct a finite-dimensional approximation to the linear dynamics given by Eqn. (2.32) and to the quadratic spatial integration term in the cost-functional (Eqn. (2.39)). The variational Hamiltonian for the resulting linear quadratic control problem is given by

$$H(\mathbf{w}^N, \mathbf{u}^N, \lambda^N) = (\mathbf{w}^N)^T \mathbf{Q}^N \mathbf{w}^N / 2 + (\mathbf{u}^N)^T \mathbf{R}^N \mathbf{u}^N / 2 + (\lambda^N)^T \left(\mathbf{A}^N \mathbf{w}^N + \mathbf{B}^N \mathbf{u}^N \right), \quad (2.40)$$

where λ^N is the Lagrange multiplier. The solution to the steady Riccati equation yields a matrix $\mathbf{P}^N$ which maps the state onto the Lagrange multiplier through

$$\lambda^N = \mathbf{P}^N \mathbf{w}^N. \quad (2.41)$$

The steady Riccati equation is a result of the usual necessary optimality conditions for this linear-quadratic regulator problem (see Paraskevopoulos [12]). For notational economy at this point we omit the superscript N. For the remainder of this section we deal only with the finite-dimensional problem.

The Riccati matrix $\mathbf{P}$ is the unique positive-definite solution of

$$\mathbf{PA} + \mathbf{A}^T \mathbf{P} - \mathbf{PBR}^{-1} \mathbf{B}^T \mathbf{P} + \mathbf{Q} = 0. \quad (2.42)$$

In our application, the Riccati equation is solved using `matlab`, and the control is given by

$$\mathbf{u} = -\mathbf{R}^{-1} \mathbf{B}^T \lambda = -\mathbf{R}^{-1} \mathbf{B}^T \mathbf{P} \mathbf{w} = -\mathbf{K} \mathbf{w}. \quad (2.43)$$

The matrix, $\mathbf{K}$, is called the Kalman matrix or the gain matrix.

Feedback control: Numerical results

We shall consider the cost functional (Eqn. (2.39)) with the following weights $Q_\rho(x) = 0$, $Q_u(x) = 0.1$, $Q_p(x) = 1$ and $R = 10^3$. These weights are somewhat arbitrary but reflect the fact that we want to limit the pressure oscillations and that in the open-loop simulations the velocity responses are noticeably smaller than the pressure responses. In this low-Mach flow, density changes are expected to be small.

The feedback control is applied to linear and non-linear systems. The pressure response at the inflow is shown in Figure 2.44(a) for both the linear and non-linear problems. As seen in Figure 2.44(b), the control required to damp the pressure disturbances is much smaller than would be necessary to achieve thermal choking (*i.e.*, 1000).

The same control is applied to the non-linear system at time, $t = 2.0\,sec$ after the limit cycle has been established (see Figure 2.42(b)). The envelope of the pressure response at the inflow is shown in Figure 2.45. The oscillation reaches half-amplitude in approximately $0.065\,sec$ with an initial damping rate of 2.6 orders per second. For this particular finite-volume representation, the control is very effective; however, further investigation uncovers some issues of concern.

Feedback Control Pressure Response to a 1-D Bombing Pulse, $p_{out}'=0$

$\Delta p/p_\infty=1\%$, $\gamma=1.396$, $U=15\ m/s$, 2nd-Order RK, $\Delta t=10^{-5}$
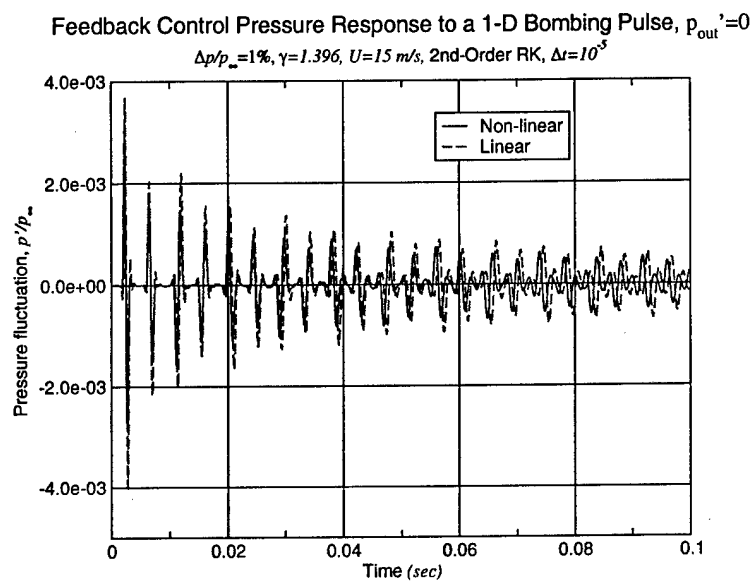
(a) Inflow pressure response to feedback control.

Control of a 1-D Bombing Pulse, $p_{out}'=0$

$\Delta p/p_\infty=1\%$, $\gamma=1.396$, $U=15\ m/s$, 2nd-Order RK, $\Delta t=10^{-5}$
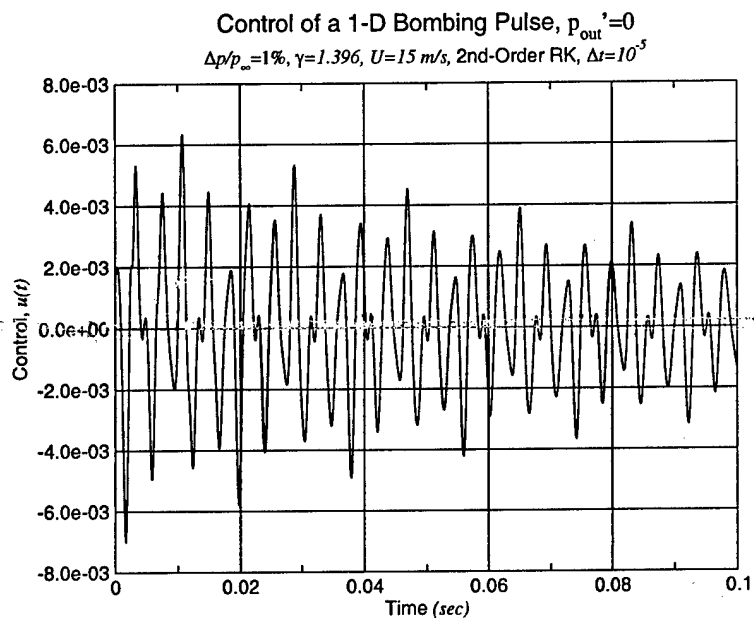
(b) Feedback control history.

Figure 2.44: Linear and non-linear feedback control response.
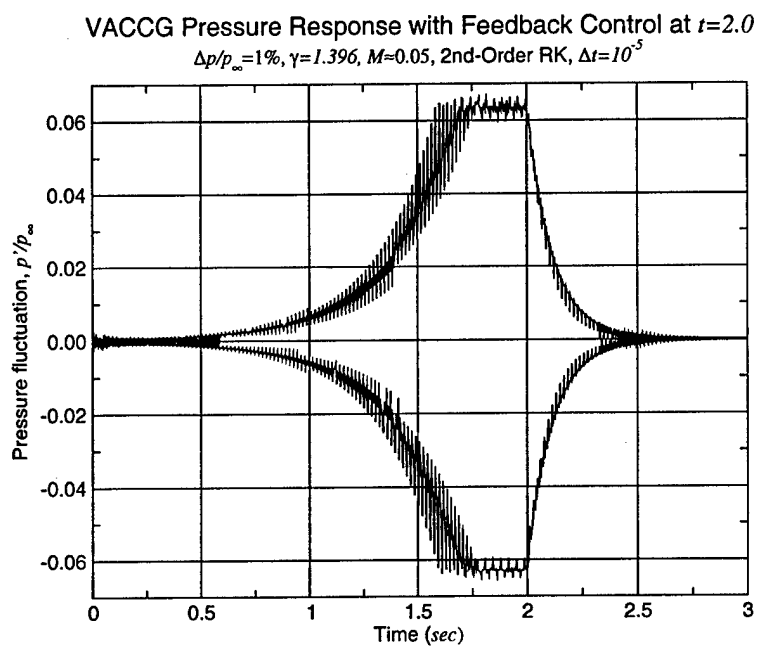
Figure 2.45: Non-linear response to feedback control applied at $t = 2.0$
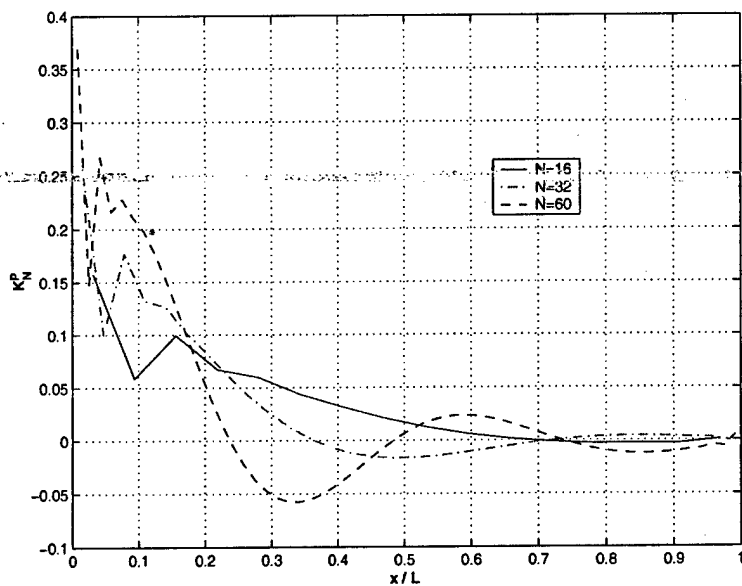
Figure 2.46: Pressure gain functional at different mesh densities.
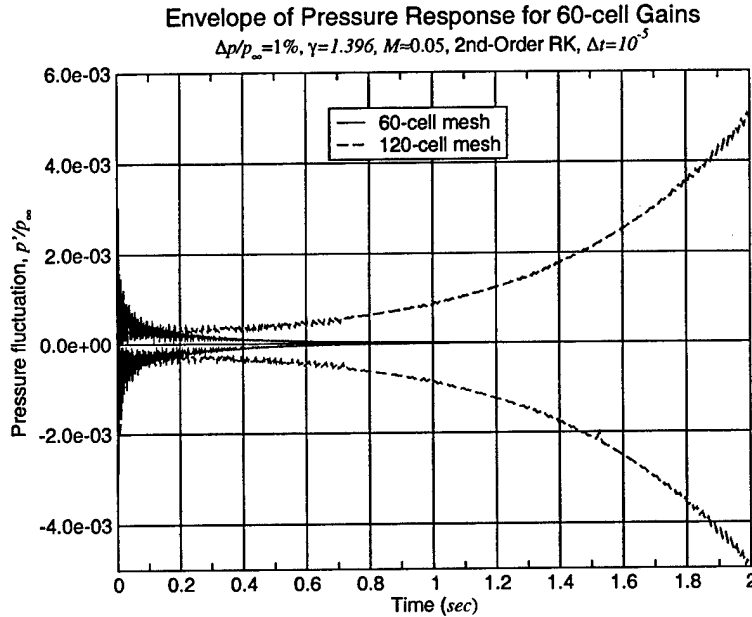
Figure 2.47: Envelope of pressure response for 60-cell gains used on a 60-cell mesh and a 120-cell mesh.

Feedback Control: Reasons for concern

Results for the pressure gain functional (K_N^p) with $N = 32, 60, 128$ are shown in Figure 2.46. Note that the number and magnitude of the oscillations is increasing as the grid is refined. This is typical of *weak convergence* and indicates a potential difficulty with our numerical approximation. Specifically, as N increases the finite-dimensional operator $\mathbf{A}_N$ must converge, in an appropriate sense, to the linear approximation of the continuum (*i.e.*, PDE) model. In addition, convergence of the gains in the LQR problem, also requires that the adjoints of the operators converge. In other application of distributed-parameter control theory, lack of adjoint convergence has led to (only) weak convergence of the functional gains.

One method to investigate gain convergence is to use the 60-cell gains on a finer mesh of 120 cells. That is, the ith gain is used on cell numbers $2i$ and $2i + 1$. If the behavior is the same, then we know that the gain is grid-converged – the converse is also true. A plot of the pressure-response envelope is given in Figure 2.47 which shows that the 120-cell case is unstable even with control.

Distributed Parameter Systems

In the previous sections, we have described a non-linear finite-dimensional (ODE) model based on a finite-volume approximation to the flow equations. The non-linear ODE model was linearized and used to construct a stabilizing controller based on an linear-quadratic regulator (LQR). For this specific discretization the state-feedback controller was shown to stabilize the non-linear ODE model. However, the linear controller applied to a non-linear ODE model based on a finer discretization did not result in a stable system. Moreover, as the finite-dimensional model is refined, calculations performed on the sequence of linear

control problems indicate that certain *functional gains* for the DPS model apparently fail to converge. Thus, we are interested in constructing a linear distributed-parameter model and studying control and approximation issues.

2.4.1 Units and Scaling

Next, we introduce non-dimensional time and length variables given by

$$\hat{t} = \frac{t}{L/u_0}, \quad \text{and} \quad \hat{x} = \frac{x}{L},$$

and a non-dimensional mass variable given by

$$\hat{m} = \frac{m}{\rho_0 L^3}.$$

In these expressions u_0 and ρ_0 are convenient values of flow velocity and density. The scaled versions of the (primitive) dependent variables are

$$
\begin{aligned}
\hat{\rho}(\hat{t}, \hat{x}) &= \rho(\hat{t}L/u_0, \hat{x}L)/\rho_0 \\
\hat{u}(\hat{t}, \hat{x}) &= u(\hat{t}L/u_0, \hat{x}L)/u_0 \\
\hat{p}(\hat{t}, \hat{x}) &= p(\hat{t}L/u_0, \hat{x}L)/(\rho_0 u_0^2).
\end{aligned}
$$

The linearized PDE for the scaled primitive variables is

$$
\frac{\partial}{\partial \hat{t}}
\begin{bmatrix} \hat{\rho} \\ \hat{u} \\ \hat{p} \end{bmatrix} (\hat{t}, \hat{x})
+
\begin{bmatrix} 1 & 1 & 0 \\ 0 & 1 & 1 \\ 0 & 1/M_0^2 & 1 \end{bmatrix}
\frac{\partial}{\partial \hat{x}}
\begin{bmatrix} \hat{\rho} \\ \hat{u} \\ \hat{p} \end{bmatrix} (\hat{t}, \hat{x})
=
\begin{bmatrix} 0 \\ 0 \\ (\gamma - 1)\hat{S}_e(\hat{t}, \hat{x}) \end{bmatrix},
\qquad (2.44)
$$

where

$$\hat{S}_e(\hat{t}, \hat{x}) = \frac{L}{\rho_0 u_0^3} S_e(\hat{t}L/u_0, \hat{x}L).$$

2.4.2 Boundary Conditions

Classical characteristic analysis of Euler flows suggests that for subsonic flows one should provide two (Dirichlet) conditions at the inflow and one at the outflow. In our case one of the inflow conditions is used to model unsteady combustion features that are not otherwise described.

Inflow Conditions

At $\hat{x} = 0$ the mathematical boundary conditions are:

- mass flow change proportional to pressure change

$$\frac{d(\rho u)}{\rho^0 u^0} = \alpha \frac{dp}{p^0}, \text{ and}$$

- constant entropy ($\frac{p(t,0)}{\rho(t,0)^\gamma} = K$).

In terms of our scaled perturbation variables, the first condition leads to

$$\hat{u}(\hat{t}, 0) + \hat{\rho}(\hat{t}, 0) - \frac{\alpha}{(p_0/\rho_0 u_0^2)} \hat{p}(\hat{t}, 0) = 0, \qquad (2.45)$$

while the second condition leads to

$$M_0^2 \hat{p}(\hat{t}, 0) - \hat{\rho}(\hat{t}, 0) = 0. \qquad (2.46)$$

Outflow Conditions

At the outflow $\hat{x} = 1$ the only boundary condition is

- fixed pressure $(p(t, L) = p_0)$,

which leads to the simple requirement

$$\hat{p}(\hat{t}, 1) = 0. \qquad (2.47)$$

2.5   Abstract (DPS) Model

We begin with the Hilbert space $\mathcal{Z} = L_2([0, 1], \mathbb{R}^3)$, which consists (essentially) of continuous functions on the unit (spatial) interval with values in $\mathbb{R}^3$. To incorporate boundary conditions we define the matrices

$$B_L = \begin{bmatrix} 1 & 1 & -\tilde{\alpha} \\ -1 & 0 & M_0^2 \end{bmatrix}, \qquad (2.48)$$

$$B_R = \begin{bmatrix} 0 & 0 & 1 \end{bmatrix}, \qquad (2.49)$$

where $\tilde{\alpha} = \frac{\alpha}{(p_0/\rho_0 u_0^2)}$ (see Eqn. 2.45).

One approach is to build the boundary conditions into the domain of the operator. Define the operator $\mathcal{A} : D(\mathcal{A}) \mapsto \mathcal{Z}$ with domain:

$$D(\mathcal{A}) = \left\{ \psi \in \mathcal{Z} \,|\, \psi \text{ is a.c., } \psi' \in L_2, B_L \psi(0) = 0 \in \mathbb{R}^2, B_R \psi(1) = 0 \in \mathbb{R} \right\}$$

and with action given by:

$$[\mathcal{A}\psi](x) = -\underbrace{\begin{bmatrix} 1 & 1 & 0 \\ 0 & 1 & 1 \\ 0 & 1/M_0^2 & 1 \end{bmatrix}}_{\equiv A} [\psi'](x). \qquad (2.50)$$

The homogeneous case of Eqn. (2.44) can then be written as

$$\dot{z}(t) = \mathcal{A}z(t),$$

and we need to show that $\mathcal{A}$ generates a C_0 semigroup on $\mathcal{Z}$.

One possible approach is to use a theorem from Pazy [13, see Theorem 5.3, page 20]. This requires that we show that

1. $\mathcal{A}$ is closed and densely defined,

2. there exists real numbers $M > 0$ and ω so that the resolvent set includes the ray (ω, ∞), and the resolvent operator $R(\lambda, \mathcal{A})$ satisfies the inequality

$$\|R(\lambda, \mathcal{A})^n\| \leq \frac{M}{(\lambda - \omega)^n},$$

for $\Re(\lambda) > \omega$, and $n = 1, 2, \ldots$.

2.5.1 Characterizing the spectrum of $\mathcal{A}$

From Eqn. (2.50) we have $[\mathcal{A}\psi](x) = -A\psi'(x)$, so that for λ an eigenvalue of $\mathcal{A}$, we must have

$$\psi'(x) = -\lambda A^{-1}\psi(x),$$

where, for the moment, we assume that A is invertible. From this expression we have the representation

$$\psi(x) = \exp\left(-\lambda A^{-1} x\right)\psi(0).$$

The boundary conditions (2.48, 2.49), then imply that

$$\underbrace{\begin{bmatrix} B_L \\ B_R \exp\left[-\lambda A^{-1}\right] \end{bmatrix}}_{\equiv M(\lambda)} \psi(0) = 0 \in \mathbb{R}^3. \qquad (2.51)$$

Hence, eigenvalues of the operator $\mathcal{A}$ are equivalently eigenvalues of the matrix $M(\lambda)$.

To construct the required matrix exponential we use standard results from one-dimensional Euler flow analysis for a spectral representation of the matrix A. Specifically, from [14, see pages 158, ff] the eigenvalues of A are

$$\sigma_1 = 1, \quad \sigma_2 = 1 + 1/M_0, \quad \sigma_3 = 1 - 1/M_0.$$

Note, in particular, that for $0 < M_0 < 1$, the matrix A is well-defined and invertible. Additionally, right eigenvectors (u_i) of A are given by the columns of the matrix

$$L = \begin{bmatrix} 1 & M_0/2 & -M_0/2 \\ 0 & 1/2 & 1/2 \\ 0 & 1/(2M_0) & -1/(2M_0) \end{bmatrix},$$

while the reciprocal left eigenvectors (v_i^T) are given by the rows of

$$L^{-1} = \begin{bmatrix} 1 & 0 & -M_0^2 \\ 0 & 1 & M_0 \\ 0 & 1 & -M_0 \end{bmatrix}.$$

Since A is invertible, it follows that the eigenvalues of A^{-1} are the reciprocals of the corresponding eigenvalues of A while the right (left) eigenvectors of the two matrices are the same. From these observations it follows that

$$\exp\left[-\lambda A^{-1}\right] = \sum_{i=1}^{3} \exp(-\lambda/\sigma_i) u_i v_i^T.$$

Using the expressions for $B_R, \sigma_i, u_i,$ and v_i, it can be shown that the last row of the matrix $M(\lambda)$ in Eqn (2.51) is

$$\left[\ 0 \quad M_{32}(\lambda) \quad M_{33}(\lambda)\ \right],$$

where,

$$M_{32}(\lambda) = \frac{1}{2M_0}\left(\exp\left(\frac{-M_0\lambda}{1+M_0}\right) - \exp\left(\frac{M_0\lambda}{1-M_0}\right)\right),$$

and

$$M_{33}(\lambda) = \frac{1}{2}\left(\exp\left(\frac{-M_0\lambda}{1+M_0}\right) + \exp\left(\frac{M_0\lambda}{1-M_0}\right)\right).$$

From this it follows that the characteristic function for $M(\lambda)$ is

$$c(\lambda) = \left(\tilde{\alpha} + M_0 - M_0^2\right)\exp\left(\frac{-M_0\lambda}{1+M_0}\right) - \left(\tilde{\alpha} - M_0 - M_0^2\right)\exp\left(\frac{M_0\lambda}{1-M_0}\right). \qquad (2.52)$$

2.5.2 Roots of the Characteristic Equation

Define

$$
\begin{aligned}
c_1 &= \tilde{\alpha} + M_0 - M_0^2 \\
c_2 &= \tilde{\alpha} - M_0 - M_0^2,
\end{aligned}
$$

and note that $c_1 > c_2$. Additionally, define

$$a = \frac{M_0}{1+M_0} \quad \text{and} \quad b = \frac{M_0}{1-M_0}.$$

Recall that $0 < M_0 < 1$ so that $b > a > 0$. We write $\lambda = \sigma + i\omega$ and the characteristic equation $(c(\lambda) = 0)$ leads to

$$c_1\exp(-a\sigma)\cos(a\omega) - c_2\exp(b\sigma)\cos(b\omega) = 0 \qquad (2.53)$$
$$c_1\exp(-a\sigma)\sin(a\omega) + c_2\exp(b\sigma)\sin(b\omega) = 0 \qquad (2.54)$$

Note that if $\cos(a\omega) = 0$ then we must have $\cos(b\omega) = 0$ so that b/a is rational. We **assume** that this does not occur in the generic case (*i.e.* $\cos(a\omega)\cos(b\omega) \neq 0$). From equations (2.53, 2.54) it follows that

$$\tan(a\omega) + \tan(b\omega) = 0. \qquad (2.55)$$

Note that any solution of the characteristic equation is a solution of (2.55), but **not conversely**. In our generic case we use the trigonometric identity

$$\tan(a\omega) + \tan(b\omega) = \tan((a+b)\omega)(1 - \tan(a\omega)\tan(b\omega)),$$

where we have assumed that $\cos((a+b)\omega)$ is non-zero. From Eqn (2.55) it follows that $\tan(a\omega)\tan(b\omega) \leq 0$, so that the last factor is is not zero, which implies that $\tan((a+b)\omega) = 0$, or that

$$\omega_k = \frac{k\pi}{(a+b)}, \quad k = 0, 1, \ldots \qquad (2.56)$$

Eqn (2.57)		$N = 60$		$N = 128$		$N = 256$	
σ_k	ω_k	σ_k	ω_k	σ_k	ω_k	σ_k	ω_k
.3905	34.45	.387	34.1	.392	34.3	.394	34.4
.3905	103.35	.357	102.2	.386	102.8	.392	103.1
.3905	172.26	.276	170.3	.371	171.4	.389	171.8
.3905	241.17	.108	238.5	.344	239.9	.383	240.5

Table 2.3: First four modes

Next, observe that

$$a\omega_k = k\pi - b\omega_k,$$

so that

$$\cos(a\omega_k) = (-1)^k \cos(b\omega_k) \implies \frac{\cos(a\omega_k)}{\cos(b\omega_k)} = (-1)^k,$$

and, similarly that

$$\frac{\sin(a\omega_k)}{\sin(b\omega_k)} = (-1)^{k+1}.$$

Clearly, $\cos((a+b)\omega_k)$ is non-zero. With ω_k values from (2.56) we formally use Eqns (2.53, 2.54) to solve for σ. The results are

$$\sigma_k^c = \log\left(\frac{c_1}{c_2}\frac{\cos(a\omega_k)}{\cos(b\omega_k)}\right)/(a+b)$$

$$\sigma_k^s = \log\left(-\frac{c_1}{c_2}\frac{\sin(a\omega_k)}{\sin(b\omega_k)}\right)/(a+b).$$

In the case $c_1/c_2 < 0$ only the odd values of k yield real values of σ_k, while in the case if $c_1/c_2 > 0$, only the even values of k are appropriate. Finally, if $c_1 = 0$ or $c_2 = 0$, the spectrum of $\mathcal{A}$ is empty. With $M_0 > 0$ the case $c_1 = c_2 = 0$ cannot occur. In summary, we have

$$\lambda_\ell = \frac{\log(|c_1/c_2|) \pm i(2\ell + \delta)\pi}{(a+b)}, \quad \ell = 0, 1, 2, \ldots, \tag{2.57}$$

where

$$\delta = \begin{cases} 0 & \text{if } c_1/c_2 > 0 \\ 1 & \text{if } c_1/c_2 < 0 \end{cases}$$

These calculations are compared to values from the the LQR model for the case: $\tilde{\alpha} = .00288$ and $M_0 = .0455$. Note that $b/a \approx 2091/1909$. In summary, we find

$$\lambda_\ell \approx .124 \pm i34.45(2\ell + 1), \quad \ell = 0, 1, \ldots$$

Table (2.3) presents a comparison of the predictions for the first four modes from Eqn (2.57) and from the LQR methods described earlier.

2.5.3 A Few Interesting Limits

- Neutral stability ($\Re(\lambda_\ell) = 0$) occurs when $|c_1/c_2| = 1$, or $c_2 = -c_1$. This implies that $\tilde{\alpha} = M_0^2$ or $\alpha = 1/\gamma$.

- As $c_1 \downarrow 0$ we have $\Re(\lambda_\ell) \to -\infty$. This occurs as $\alpha \downarrow -\frac{1-M_0}{\gamma M_0}$. At $c_1 = 0$, the operator $\mathcal{A}$ has empty spectrum.

- As $c_2 \uparrow 0$ we have $\Re(\lambda_\ell) \to \infty$. This occurs as $\alpha \uparrow \frac{1+M_0}{\gamma M_0}$. At $c_2 = 0$, the operator $\mathcal{A}$ has empty spectrum.

2.5.4 Resolvent of $\mathcal{A}$

As notes at the beginning of the Section (see page 59), well-posedness of the model can be established through certain bounds on the resolvent operator. Thus, it is of interest to provide a representation of this resolvent operator. We have performed this analysis but omit it from the current report.

2.6 Boundary Control

The physical system may admit the possibility of control through the flame dynamics. Our simplified analysis treats the fluid as a perfect-gas, while the flame is modelled through the inflow boundary conditions (see Section 2.4.2).

Following ideas presented in [15] we generalize the mass in-flow boundary condition (2.45) to

$$\hat{u}(t, 0) + \hat{p}(t, 0) - y_p(t, 0) - y_c(t, 0) = 0, \tag{2.58}$$

where $y_p(t)$ is the scalar output of a finite-dimensional linear system driven by the pressure perturbation at the inflow boundary, and $y_c(t)$ is the scalar output of a finite-dimensional linear system driven by an exogenous control.

For the pressure driven system we have

$$\dot{\mu}_p(t) = A_p \mu_p(t) + e_k \hat{p}(t, 0) \tag{2.59}$$

$$y_p(t) = C_p \mu_p(t) + \frac{\alpha}{(p_0/\rho_0 u_0^2)} \hat{p}(t, 0), \tag{2.60}$$

where $\mu_p(t) \in \mathbb{R}^k$. Without loss of generality, we can assume the system is in control-canonical form, so that, for example, e_k is the k column vector with zeros except for unity in the last entry. The transfer function for the system (2.59, 2.60) is

$$G_p(s) = \frac{Y_p(s)}{P(s)} = \frac{c_p^1 + c_p^2 s + \ldots + c_p^k s^{(k-1)}}{d_p^1 + d_p^2 s + \ldots + d_p^k s^{(k-1)} + s^k} + \frac{\alpha}{(p_0/\rho_0 u_0^2)}. \tag{2.61}$$

Note that by choosing $c_p^\jmath = 0$, $\jmath = 1, 2 \ldots, k$ we recover the original pressure contribution from Eqn (2.45).

Contributions from the (new) control term ($v(t)$) are modelled similarly

$$\dot{\mu}_c(t) = A_c \mu_p(t) + e_\ell v(t) \tag{2.62}$$

$$y_c(t) = C_c \mu_c(t), \tag{2.63}$$

where $\mu_c(t) \in \mathbb{R}^\ell$. The transfer function for the system (2.62, 2.63) is

$$G_c(s) = \frac{Y_c(s)}{V(s)} = \frac{c_c^1 + c_c^2 s + \ldots + c_c^\ell s^{(\ell-1)}}{d_c^1 + d_c^2 s + \ldots + d_c^\ell s^{(\ell-1)} + s^\ell}. \tag{2.64}$$

For technical reasons G_c is strictly proper; there is no direct $v(t) \mapsto y_c(t)$ connection.

2.6.1 Second Abstract (DPS) Model

Define the Hilbert space $\mathcal{W} = \mathbb{R}^\ell \times \mathbb{R}^k \times \mathcal{Z}$ with elements $w = (\mu_c, \mu_p, \psi)$. The 2nd abstract model is given by

$$\dot{w}(t) = \mathcal{A}_w w(t) + b_w v(t), \tag{2.65}$$

where the operator $\mathcal{A}_w : D(\mathcal{A}_w) \mapsto \mathcal{W}$ has domain:

$$D(\mathcal{A}_w) = \Big\{ \mu_c \in \mathbb{R}^\ell, \mu_p \in \mathbb{R}^k, \psi \in \mathcal{Z} | \psi \text{ is a.c., } \psi' \in L_2,$$

$$- C_c \mu_c - C_p \mu_p + \psi_1(0) + \psi_2(0) - \tilde{\alpha} \psi_3(0) = 0,$$

$$-\psi_1(0) + M_0^2 \psi_3(0) = 0, \quad \psi_3(1) = 0 \Big\}$$

and action given by:

$$\mathcal{A}_w \begin{bmatrix} \mu_c \\ \mu_p \\ \psi \end{bmatrix} = \begin{bmatrix} A_c \mu_c \\ A_p \mu_p + e_k \psi_3(0) \\ -A\psi' \end{bmatrix}, \tag{2.66}$$

where the 3×3 matrix A has been defined in Eqn (2.50). The control operator $b_w : \mathbb{R} \mapsto \mathcal{W}$ is given by

$$b_w v = \begin{bmatrix} e_\ell v \\ 0 \\ 0 \end{bmatrix}. \tag{2.67}$$

A block diagram of the system is shown in Figure 2.48. The dark vertical bar is a *MUX* operator; the output vector concatenates the input vectors.

2.6.2 Characterizing the spectrum of $\mathcal{A}_w$

From the definition of the operator $\mathcal{A}_w$ in Eqn (2.66), if λ is an eigenvalue we must have

$$A_c \mu_c = \lambda \mu_c \tag{2.68}$$

$$A_p \mu_p + e_k \psi_3(0) = \lambda \mu_p \tag{2.69}$$

$$-A\psi' = \lambda \psi. \tag{2.70}$$

As in Section 2.5.1, Eqn (2.70) implies that

$$\psi(x) = \exp\left(-\lambda A^{-1} x\right) \psi(0).$$

This representation, combined with the boundary conditions and Eqns (2.68, 2.69) leads to

$$\underbrace{\begin{bmatrix} \lambda I - A_c & 0 & 0 \\ 0 & \lambda I - A_p & e_k[0\ 0\ 1] \\ -C_c & -C_p & \\ 0 & 0 & M(\lambda) \\ 0 & 0 & \end{bmatrix}}_{\equiv \hat{M}(\lambda)} \begin{pmatrix} \mu_c \\ \mu_p \\ \psi(0) \end{pmatrix} = 0 \in \mathbb{R}^{\ell+k+3}, \tag{2.71}$$

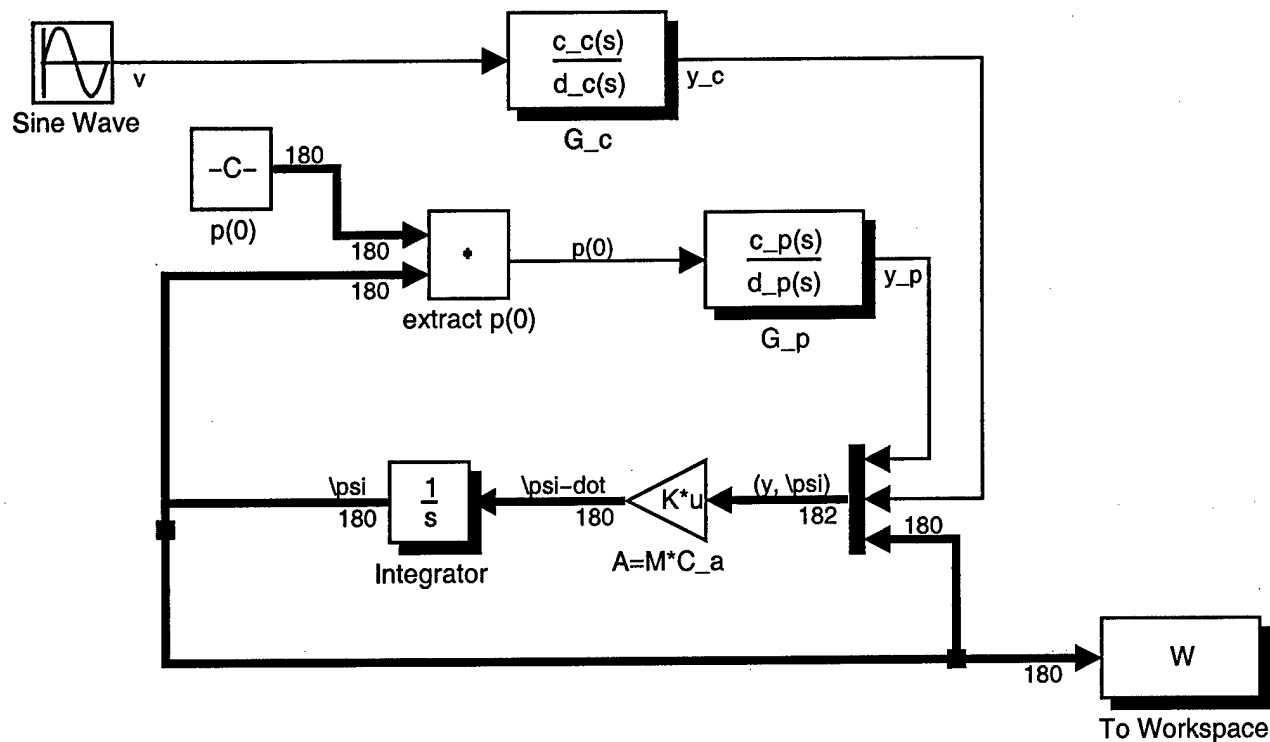Figure 2.48: MATLAB SIMULINK Block Diagram

where the lower-right 3×3 block $(M(\lambda))$ has been defined in Eqn (2.51). We are interested in characterizing the eigenvalues of the matrix $(\hat{M}(\lambda))$ on the left-side of Eqn (2.71). Note that eigenvalues of A_c that are distinct from the eigenvalues of the lower right $(k+3) \times (k+3)$ block, are also eigenvalues of $\hat{M}(\lambda)$.

Bibliography

[1] C. T. Bowman and D. J. Seery. "Investigation of NO Formation Kinetics in Combustion Processes: The Methane-Oxygen-Nitrogen Reaction". In W. Cornelius and W. G. Agnew, editors, **Emissions for Continuous Combustion Systems**, pages 123–139. Plenum Press, 1972.

[2] P. R. Spalart and S. R. Allmaras. A One-Equation Turbulence Model for Aerodynamic Flows. AIAA Paper 92-0439, 30th *AIAA Aerospace Sciences Meeting*, January, 1992.

[3] A. G. Godfrey. *"Topics on Spatially High-Order Accurate Methods and Preconditioning for the Navier-Stokes Equations with Finite-Rate Chemistry"*. PhD thesis, Virginia Polytechnic Institute and State University, 1992.

[4] S. Eberhardt and S. Imlay. "A Diagonal Implicit Scheme for Computing Flows with Finite-Rate Chemistry". AIAA Paper 90-1577, 21st *AIAA Fluid Dynamics, Plasma Dynamics and Lasers Conference*, Seattle, Washington, June 18-20 1990.

[5] S. R. Turns. **An Introduction to Combustion**. McGraw-Hill, 2000.

[6] S.-W. Kang, M. G. Dunn, and W. L. Jones. "Theoretical and Measured Electron-Density Distributions for the RAM Vehicle at High Altitudes". AIAA Paper 72-689, *AIAA 5th Fluid and Plasma Dynamics Conference*, June, 1972.

[7] A. G. Godfrey and E. M. Cliff. "Sensitivity Equations for Turbulent Flows". AIAA Paper 2001-1060, 39th *AIAA Aerospace Sciences Meeting and Exhibit*, January 8-11, 2001.

[8] J. R. Appel and M. D. Gunzburger. "Difficulties in Sensitivity Calculations for Flow with Discontinuities". *AIAA Journal*, **35**(5):842–848, 1997.

[9] S. Venkateswaran, J. Grenda, and C. L. Merkle. "Computational Fluid Dynamic Analysis of Liquid Rocket Combustion Instability". AIAA Paper 91-1609, 22nd *AIAA Fluid Dynamics, Plasma Dynamics and Lasers Conference*, Honolulu, Hawaii, June 24-26 1991.

[10] Z. J. Wang, H. Q. Yang, and A. J. Przekwas. "Assessment of Total Variation Diminshing Schemes in Combustion Instability Problems". AIAA Paper 93-0111, *AIAA 31st AIAA Aerospace Sciences Meeting and Exhibit*, January 11-14 1993.

[11] J. D. Anderson. **Modern Compressible Flow: With Historical Perspective**. McGraw-Hill Book Company, 1982.

[12] P. N. Paraskevopoulos. **Modern Control Engineering**. Marcel Dekker, New York, 2002.

[13] A. Pazy. **Semigroups of linear operators and applications to partial differential equations**. Springer-Verlag, New York, 1983.

[14] C. Hirsch. **Numerical Computation of Internal and External Flows, Volume 2**. John Wiley and Sons, New York, 1990.

[15] G. Poncia. *" A Study of Thermoacoustic Instability Phenomena in Combustion Chambers or Active Control"*. PhD thesis, Politecnica di Milano, 1999.